Estimation of mud and sand fractions and total concentration from coupled optical-acoustic sensors

Duc Tran[1,3], Matthias Jacquet[1], Stuart Pearson[2], Bram Van Prooijen[2] and Romaric Verney[1]

[1] IFREMER, DYNECO/DHYSED, ZI pointe du Diable, CS10070 Plouzane, France

[2] Faculty of Civil Engineering and Geosciences, Delft University of Technology, P.O. Box 5048, 2600GA, Delft, the Netherlands

[3] Current: Royal Belgian Institute of Natural Sciences, OD Nature, Rue Vautier 29, 1000 Brussels, Belgium

ABSTRACT

Optical and acoustic sensors have been widely used in laboratory experiments and field studies to investigate suspended particulate matter concentration and particle size over the last four decades. Both methods face a serious challenge as laboratory and in-situ calibrations are usually required. Furthermore, in coastal and estuarine environments, the coexistence of mud and sand often results in multimodal particle size distributions, amplifying erroneous measurements. This paper proposes a new approach of combining a pair of optical-acoustic signals to estimate the total concentration and sediment composition of a mud/sand mixture in an efficient way without an extensive calibration. More specifically, we first carried out a set of 54 bimodal size regime experiments to derive empirical functions of optical-acoustic signals, concentrations, and mud/sand fractions. The functionalities of these relationships were then tested and validated using more complex multimodal size regime experiments over 30 optical-acoustic pairs of 5 wavelengths (420, 532, 620, 700, 852 nm) and 6 frequencies (0.5, 1, 2, 4, 6, 8 MHz). In the range of our data, without prior knowledge of particle size distribution, combinations between optical wavelengths 620-700 nm and acoustic frequencies 4-6 MHz predict mud/sand fraction and total concentration with the variation < 10% for the former and < 15%

email addresses: dtran@naturalsciences.be (Duc Tran), romaric.verney@ifremer.fr (Romaric Verney)

for the later. This approach therefore enables the robust estimation of suspended sediment concentration and composition, which is particularly useful in cases where calibration data is insufficient.

Keywords:

Acoustic, Optical, Sand, Mud, SPM concentration, DEXMES,

1 INTRODUCTION

Accurate observation of suspended particulate matter concentration (SPMC) typically requires combinations of one or more optical and acoustic sensors with gravimetric measurements of filtered water samples (Sutherland et al., 2000; Bux et al., 2019; Fettweis et al., 2019). This is because both optical and acoustic sensors indirectly measure either the attenuation/backscattered signal of an optical beam or the acoustic backscatter as a proxy of SPMC. Conversely, the gravimetric measurements of filtered water samples directly provide the ground truth reference of SPMC. A regression model is then developed based on these indirect measurements and direct measurements of SPMC (Fettweis et al., 2019). Both direct or indirect measurements of SPMC have their own drawbacks. Physical water sampling is often impractical and expensive, particularly at high-frequencies over long periods for timeseries or vertical profile data collections. Optical and acoustic methods, on the other hand, provide high-resolution measurements. However, these two methods demand laboratory and *in-situ* calibration owing to the strong dependence of the backscattering characteristics on mineralogical compositions, particle size, density and shape (Slade et al., 2011; Salehi and Strom, 2011; Doxaran et al., 2016; Druine et al., 2018). The backscattering signal is also influenced by the presence of salinity, bubbles and biological fouling (Downing, 2006; Salehi and Strom, 2011; Sahin et al., 2017; Bux et al., 2019; Haalboom et al., 2021). In practice, optical and acoustic measurements often combine with several *in-situ* or laboratory calibrations of water samples obtained from the field. For reliable and high fidelity data, it is suggested that sensors need to be re-calibrated with water samples when there are significant changes in SPM compositions and/or hydrodynamics conditions (Moura et al., 2011; Fettweis et al., 2019; Pearson et al., 2021; Haalboom et al., 2021). Hence, these methods require not only site-specific but also instrument-specific calibrations, adding another layer of difficulty and uncertainty to the inversion process.

Particles in suspension respond to both optical and acoustic signals via a similar mechanism, albeit to different degrees. Optical sensors illuminate a water sample volume with a light source, then the photodetectors convert either the optical beam attenuation or back(side)scatter intensity of the light in voltage or turbidity units (Downing, 2006; Fettweis et al., 2019). Similarly, acoustic sensors indirectly estimate concentration by quantifying the changes in backscattered acoustic signals, in dB (Sahin et al., 2017; Bux et al., 2019; Haalboom et al., 2021). The peak sensitivity of acoustic backscatter signal to particle size occurs at upper limit of the Rayleigh regime at $2\pi r\lambda^{-1} \approx 1$ (Downing, 2006; Thorne and Hurther, 2014; Haalboom et al., 2021), where r is the particle radius and λ is the acoustic wavelength. For example, an Acoustic Doppler Velocimeter (ADV) working at 2 or 6 MHz will have the best performance with sand particles at sizes of 240 or 80 μm, respectively. For optical backscatter sensors, the light scattering and refractive index are largely dictated by the number of illuminated particles, or total illuminated areas (Downing, 2006), hence, the optical sensors are more sensitive to finer particles, i.e., mud ($d_{50} < 63$ μm). If we combine both optical and acoustic sensors in one measurement of the same suspension we would thus “see” the mud better and “hear” the sand better. This allows us to gain deeper understanding about the suspension than we could if we only use a single type of sensor (Pearson et al., 2021; Livsey et al., 2023).

This study focuses on proposing a new method to use coupled optical-acoustic measurements to infer SPM compositions and concentrations without or with limited water sampling calibrations. As discussed above, optical backscattering signals are highly sensitive to mud, and acoustic backscattering signals are highly sensitive to sand particles, and vice versa. We further hypothesize that SPMC and composition can be differentiated and calculated based on such sensitivities and differences in behaviors of mud and sand to different types of signals, i.e., optical and acoustic. The first objective of this paper is to investigate the possibility of combining a pair of optical and acoustic sensors to provide information about the mud/sand fraction and SPMC. To do so, we will quantify the sensitivity of a wide range of commercially available optical and acoustic sensors to the evolution of suspensions from mud-dominant to sand-dominant settings. More specifically, five optical and acoustic sensors will be used to cover the wavelengths from 420 to 852 nm and frequencies from 0.5 to 8 MHz, resulting in 30 different pairs of one wavelength and one frequency for each experiment. The second objective is to quantify at which wavelength/frequency the pair of optical and acoustic sensors will provide the most accurate estimation of SPMC at given concentration and particle size characteristics.

2 EXPERIMENTAL SETUP AND DATA PROCESSING

2.1 Experimental setup

Two sets of experiments were conducted to test and validate the hypothesis. The first set, the Calibration set (C_{set}) consisting of 54 experiments, was examined to derive empirical relationships between each pair of optical/acoustic signal and mud/sand fraction (f_{mud}) and concentration. The second set, the Validation set (V_{set}) used 6 experiments to justify the applicability of such empirical relationships in predicting f_{mud} and SPMC of the suspension.

Table 1 shows the experimental conditions in C_{set}. In this study, Bentonite and two particle sizes of sand were utilized to represent mud and sand. The sands were sieved with sieve mesh 100 – 125 μm and 200 – 250 μm to obtain sand S1 (d_{50} = 110 μm) and S2 (d_{50} = 240 μm), respectively. Five ratios of mud/sand fractions, f_{mud}, were investigated: pure Bentonite (f_{mud} = 100%), pure sand (f_{mud} = 0%), and three intermediate mixtures: 75, 50, 25%. Hereafter, the suffixes 1 and 2 refer to the sand particle sizes of S1 (d_{50}= 110 μm) and S2 (d_{50}= 240 μm), respectively. The suffixes _100, _75, _50, _25, _0 refer to the fraction of Bentonite in suspension, or f_{mud}. For example, C1_75 indicates the experiment from calibration set, C_{set}, in which the suspension consists of Bentonite and sand S1 with the ratio of mud/sand, f_{mud}, is 75%. For each SPM content condition, 6 concentrations were tested stepwise from 15 to 200 mg/L (Table

1). We processed the data from C_{set} as three populations which are 1) **C1**: pure Bentonite and all S1-related experiments 2) **C2**: pure Bentonite and all S2-related experiments and 3) combination of C1 and C2 called **C12**. In this study, there was only one pure Bentonite experiment; however, for consistency it was referred as C1_100 in C1 and C2_100 in C2, respectively.

Table 2 provides details of 6 additional experiments in V_{set}. It is noted that while C_{set} is a bimodal particle size mixture, V_{set} is a multimodal particle size mixture. In fact, V_{set} was split in a way that either Bentonite, S1, or S2 was the dominant sediment in various mixture ratios among the three types of sediments at least once. Thus, results from V_{set} provide not only a higher range of concentrations but also an expanded range of f_{mud}. In Table 2, the numbers outside the parentheses refers to the targeted concentrations or Bentonite fraction, f_{mud}. The numbers inside the parentheses refer to the true values of the parameters. These numbers were often less than the targeted concentrations because the applied turbulent shear was not high enough to keep all the sand in suspension at the elevation of the sensors, especially S2 (d_{50} = 240 μm).

Table 3 summarizes all the optical and acoustic sensors used in this study. Specifically, the sensors are HydroScat-4 with four channels 852, 620, 532, 420 nm, Wetlabs_FLNTU 700 nm, Laser In-Situ Scattering and Transmissometery - Acoustic Backscatter Sensor (LISST-ABS) 8 MHz, Nortek Vector Acoustic Doppler Velocimeter (ADV) 6 MHz, AQUAscat-1000R with four transducers 4, 2, 1, and 0.5 MHz. In this study, the sensors were setup so that the measuring volume of each sensor was at a similar level, around 26-33 cm below the water surface (Fig. 1).

All experiments were conducted in the DEXMES tank, (Dispositif EXpérimental de quantification des Matières En Suspension), a novel device which was particularly designed for SPM experiments (Tran et al., 2021). DEXMES tank provides sufficient volume, approximately 1 m^3, for several sensors to function simultaneously. In general, the tank was filled with fresh water and left overnight to reach room temperature. An experiment was started with 30 min of high shearing to remove bubbles inside the tank. In all experiments, the impeller was set at speed of 175 rotations per minute to provide high turbulent shear stress G = 30 - 100 s^{-1} in the tank

(Tran et al., 2021). For mud, Bentonite was stabilized in suspension for 30 min in a 5 L beaker with a mixer before being introduced into DEXMES. Next, a 30 min mixing was applied to provide enough time for Bentonite particles to reach equilibrium. Then, sand was added to the DEXMES tank, 5 min before data collection, to reach the targeted concentration. At the end of the 10 min recording step, one 1 L water sample was collected using a nozzle located at $\approx$ 25 cm below the water surface and 12 cm away from the wall of the tank. This procedure was repeated for all concentration levels (Table 1 and Fig. 1). In V_{set}, for better calibration of the true fractions of Bentonite, S1, and S2 in suspension instead of one 1 L water sample, three 1 L water samples were collected and analyzed.

2.2 Data processing

2.2.1 Optical and acoustic signal

All sensors started recording in real-time, continuous mode before any sediment was introduced into the tank until the last water sample was collected. For each examined condition, 10 min data was averaged and utilized in the analysis (Table 1). Preliminary experiments suggested that the numbers of spike/bad data points are negligible. Hence, there was no further transformation and/or correction of the output signals, except for Wetlabs_FLNTU where the output signal was converted from $count$ to NTU as recommended by the Sea-Bird Scientific: $NTU = 0.0484(count - 50)$. Another note is that the LISST-ABS is used with its default (factory) concentration without calibration. Thus, even though the unit of the output from the LISST-ABS is mg/L, it is still “raw signal”. In the present paper, we consider each transducer of the AQUAscat-1000R and each channel of the HydroScat-4 as individual sensor (Table 3). It is also noted that due to the nature of signal recording mechanisms, the relationships of ADV ($SNR - dB$) signal and SPMC or optical signal is a log-linear. Hence, in order to pair with ADV signal the concentration or optical data is converted via a $10\log_{10}(\,)$ function (Hoitink and Hoekstra, 2005; Salehi and Strom, 2011; Chmiel et al., 2018). Regarding AQUAscat-1000R sensor, AQUATEC suggested to use a quadratic regression between concentration and the backscatter signal (Eq. 4 – Aquatec Subsea Ltd (2012)). Subsequently, when pairing with optical or concentration data, AQUAscat signal is transformed to $AQUAscat^2_{signal}$. The primary goal of this study is to investigate the behavior of optical/acoustic signals to different SPM concentrations and compositions. We have no intention to make a comparison between different commercial sensors, henceforth, the optical and acoustic sensors will be referred as their wavelengths or frequencies rather than by names or brands (last column in Table 3).

2.2.2 Water sample

For each V_{set} condition, three 1 L water samples were collected. S2, S1, and Bentonite are separated by sieving through 125 and 63 μm sieves to obtain sand S2 and S1 on aluminum pans, and then filtered with a glass fiber filter to capture Bentonite, respectively. The separated sediments were dried in an oven at 50^{o}C in 24 hours and then weighted to measure mass concentration. There are a few notes regarding water sample data. First, in C_{set}, there were only two types of sediment, Bentonite and either S1 or S2, therefore we did not separate mud/sand in quantifying total concentration in C_{set}. Rather, the fraction and concentration of S1 or S2 in C_{set} are acquired by subtracting the f_{mud} from the total concentration. Second, mass concentration data showed that the true values of concentration for Bentonite and sand S1 are 5-10% lower than the target values or some times even 40%, for S2. This is because 1) the turbulence in the tank was not high enough to keep all the sand in suspension, particularly S2 and 2) we later found that the mesh size of the glass fiber filter (0.7 μm) was slightly bigger than the smallest particle sizes of the clay (Table 2). This is the reason why f_{mud} and concentrations in C2 and V_{set} cases were always noticeably different from the targeted values. Subsequently, for simplicity and convenience, the term f_{mud}, e.g., 100, 75, 50, 25, and 0%, actually refers to a very loose range, and sometimes even overlap, of mud/sand fraction, rather than indicating an absolute number. For example, f_{mud} = 75% implies a range of f_{mud} from around 65 to 85% instead of exact 75%. Even without reaching exact targets, we still have a broad range representative of mud/sand-dominant environments. Third, mass concentrations from three 1 L water samples in each V_{set} condition were almost the same (variations around 3%), verifying the quantification of f_{mud} in V_{set}. All calculations, data analysis, and figures are based on the true values of f_{mud}, mass of Bentonite, S1, and S2 in the mixture and total concentrations obtaining from physical water samples.

3 DERIVATION OF EMPIRICAL FUNCTIONS

In Pearson et al. (2021), we tested and validated a new concept, the Sediment Composition Index (SCI), in which the dynamics of mud/sand in suspension could be derived from optical and acoustic measurements, i.e., $SCI = 10log_{10}(OBS_{signal}) - ADV_{signal}$. The present paper further develops the SCI concept, aiming to quantify mud/sand concentration. This section uses data from C_{set} to demonstrate how f_{mud} and total concentration can be obtained from one pair of raw optical and acoustic signals. First, only one pair of optical/acoustic signals is used for demonstration. Then, the application of the same procedure to all optical/acoustic pairs is discussed.

3.1 Approach

The hypothesis under investigation is that because acoustic sensors are more sensitive to coarse sediments and optical sensors are more sensitive to mud, the sediment sensitivity differences can be used to elucidate the fraction of mud/sand in the mixture when both optical and acoustic sensors are combined in one measurement. Figure 2 reveals the relationships of signal-signal and signal-concentration in C_{set}. For better illustrations and simplicity, data from one pair of optical/acoustic sensor, ($O_{700} - A_8$), out of 30 pairs from C1 were used in Figure 2. Three observations can be made from this example. First, in Figure 2a,c,e pure mud (C1_100) and pure sand (C1_0) conditions are always the boundaries of mixed mud/sand conditions and lean toward the optical/acoustic axes, confirming that optical/acoustic sensors indeed respond better to finer/coarser sediments, respectively. Second, there is a linear relationship between signal-signal (Fig. 2a) and signal-concentration (Fig. 2c,e) of the same f_{mud}, e.g., five lines uniquely associated with five mud/sand ratios f_{mud}. In other words, the signal magnitudes of both sensors increase with the increase of concentration, yet the ratio of the optical/acoustic signal or concentration/signal remains constant. Third, theoretically, all the lines should converge to the point (0,0), which represents conditions with clear water, no turbulence shear, and no sediment. This is essentially the case in our experiments. These observations suggest that there are strong and unique relationships among raw signals, concentrations, and f_{mud}. This paper adopted the Curve Fitting Tool, provided by Matlab, to derive the relationship between signals, concentrations and f_{mud}. It is worth noting that the Curve Fitting Tool allows different functions, for consistency across all combination of sensors, we decided to choose the functions that provide highest R^2 rather than predefine a function form for a certain relationship.

Figure 2a shows the relationships between raw signals of O_{700} and A_8 from C1. As can be seen, each line in Figure 2a is associated with a certain slope or f_{mud}, indicating that the ratio of raw signals of O_{700}/A_8 is independent of concentration and only depends on the fraction of mud/sand in suspension. Subsequently, Figure 2b was produced by plotting f_{mud} against O_{700}/A_8 ratios to obtain Eq. 1. Eq. 1 demonstrates that the fraction of mud/sand in a suspension can be estimated from raw signals of O_{700} and A_8. Figure 2c,d shows the results when applying a similar procedure to A_8 signals and concentrations. A linear relationship between A_8 signals and concentrations is also seen. Eq. 2 is then achieved based on the relationship between ratio of Concentration/A_8 signals and f_{mud}. The same mechanism is applied to suspended concentrations and O_{700} signals (Fig. 2e,f), to get Eq. 3.

$$f_{mud} = 49log_{10}(O_{700}/A_8) + 127 \qquad (R^2 = 0.91) \tag{1}$$

$$(Concentration/A_8) = 0.014 f_{mud}^{1.13} + 1.95 \qquad (R^2 = 0.80) \tag{2}$$

$$(Concentration/O_{700}) = 25e^{-0.01 f_{mud}} \qquad (R^2 = 0.90) \tag{3}$$

Equations 1, 2, and 3, offer two ways to calculate total concentration. Starting with one pair of raw optical/acoustic signals:

- **Step 1:** obtain f_{mud} via Eq. 1.

- **Step 2:** f_{mud} then can be substituted to

  Eq. 2 to obtain Ca = $A_8 * (0.014 f_{mud}^{1.13} + 1.95)$ (**2a**)

  Eq. 3 to obtain Co = $O_{700} * (25 e^{-0.01 f_{mud}})$ (**2b**)

In this manuscript, Ca and Co refer to the estimated concentrations using acoustic (Eqs. 1 & 2) and optical (Eqs. 1 & 3) signals, respectively. For example, SCI-C12-Co refers to the SCI functions (Eqs 1,2,3) which were derived from the data set C12 and were used to estimate f_{mud} and concentration via **Step 1** and **2b**. It is noted that equations 1, 2, and 3 should be mathematically related. An example of a mathematical form of SCI functions is given in the Appendix A.

3.2 Application: single pair ($\mathbf{O_{700}}$, $\mathbf{A_8}$)

This section further examines the reliability and accuracy of the SCI functions. Predicted f_{mud} and total concentrations were acquired by applying equations 1, 2, and 3 to C1 data (Fig. 3). Overall, the functions underestimate f_{mud}, and concentration by 10% (Fig. 3a,b,c). There are two potential explanations for these underestimates. First, for pure mud and pure sand conditions, the differences between optical and acoustic signals are at their largest magnitudes. This is because in pure mud conditions, the optical signal is at its highest value, whereas the acoustic signal is at its lowest value. The opposite trend is seen in pure sand conditions, where the acoustic sensor is much more sensitive to changes in concentrations of sand than the optical sensor. Hence, the errors in predictions of f_{mud} in these two particular cases are relatively high, especially with extremely low or extremely high concentrations, leading to accumulated errors throughout the calculation process (Fig. 3d,h). Second, the mathematical forms, e.g., log (Eq. 1), power (Eq. 2), exponential (Eq. 3), or linear are an important factor that impacts the performance of the method. Conducting a thorough sensitivity analysis of each different mathematical form on the overall accuracy of the SCI method is out of the scope of this paper. For simplicity and consistency, we decided to choose the function that provides the highest R^2. Readers are referred to (Pearson et al., 2021) for additional information of how different functions, especially hyperbolic tangent function, dictate the performance of the method. Figure 3 also shows that the Co (Step 2b) approach provided slightly better results compared to Ca (Step 2a) approach. Specifically, Figure 3c reveals that the histogram of estimated concentrations in percentages of Co is sharper with a smaller standard deviation than that of Ca. Figure 3e,f,g also reveals these differences between the two ways of calculation, albeit the differences seem to be insignificant for this pair of O_{700} and A_8.

3.3 Application: All pairs

In the previous section, the pair (O_{700}, A_8) was used as an example to explicate the procedure of 1) derivation and calibration of SCI functions, 2) calculation of f_{mud}, and 3) calculation of total concentrations, Ca and Co. In this section, the same procedure is applied for other pairs of optical/acoustic signals as well as experimental data C12 (all combinations are in the Appendix B).

Figure 4 summarizes the results of four pairs, (O_{852} - A_6), (O_{420} - A_6), (O_{852} - A_4), and (O_{420}, A_4). Overall, Figure 4 shows similar patterns between signal-f_{mud} and signal-concentration as seen in Figure 2b,d,f which is different f_{mud} is associated with one unique ratio of optical/acoustic signal. Unlike Figure 2, Figure 4 used data from both C1 and C2 experiments. Hence, the SCI functions were derived based on the combined behaviors of S1 and S2. It is also reminded that all the sensors are working concurrently, measuring the same suspension at very similar elevation in the water column. As such, Figure 4 provides important information regarding the behavior of optical/acoustic sensors to different SPM compositions. First, for the same type of acoustic device, the SCI functions are in similar forms (Fig. 4a,b); yet, with different coefficients depending on the SPM compositions, the wavelengths and frequencies, as well as the working mechanisms of the sensors. For example, a closer examination of Figure 4a,b,e shows that the SCI functions are influenced by different wavelengths and frequencies to a greater degree than they are by particle sizes. That means that without prior knowledge of the suspension, i.e., particle sizes, it is possible to use a single SCI function to estimate f_{mud} and total concentration. Second, Figure 4a,b illustrate that moving from longer to shorter wavelengths will shift the SCI functions to the right or down. Third, due to the differences in principles of operation, the SCI functions are also different, e.g, between A_6 and A_4 in comparison to O_{852} and O_{420}. For example, Section 2.2.1 points out that the relationships between optical-A_6 is a log-linear and between optical-A_4 is a power function. This is one of the main issues when applying the SCI functions to wider range of different sensors.

Figures 5 and 6 further examine the results from C_{set}. Figure 5 presents the differences in percentage between true and estimated concentrations, i.e., between $C_{measured}$ and Ca, Co, obtained by SCI functions derived from C12 data. Figure 5 shows that majority of the error in predicting concentration falls within the range of ≈ 50%. Figure 5 also reveals that Co method across all pairs is more consistent and accurate than that of Ca. In other words, there is no remarkable difference between different optical sensors, and thus wavelengths are not a critical parameter in our case. In contrast, the choice of acoustic frequencies dictates the accuracy substantially, e.g., at 1, 2 MHz (Fig. 5g, i). This is also the reason why Optical–$A_{0.5}$ pairs were not included in Figure 5: they over/under-estimated f_{mud} and concentration in several orders of magnitudes. According to Rayleigh regime, this is expected because lower frequencies are not sensitive to the sands used in the experiments (d_{50}= 110 and 240 μm). This observation will be discussed further in Section 5. Another observation from Figure 5 is that among all wavelengths, the wavelength of 700 nm often produces larger errors (Fig. 5b, the red line). This is because of poor resolution of the O_{700}, particularly at low concentration in S2 dominating conditions, essentially provides the same output signals (< 1 NTU) despite the increase in concentration from 25 to 100 mg/L.

Figure 6 compares the performance of 1) different SCI functions derived from C12 but apply for C1, C2, and C12 data sets, separately and 2) each optical/acoustic pair in terms of bias and root mean square error (RMSE). Figure 6 confirms the observations from Figure 5 that are the Co method provides better estimation of f_{mud} and concentration than Ca method. In addition, an RMSE of 10 mg/L over a range of concentration from 15 to 200 mg/L is a relatively good prediction of concentration, especially when the knowledge of the suspension is unknown. The influence of frequencies on the Ca method is revealed via different clusters of shapes, which represent different acoustic sensors (Fig. 6a,c,e).

4 VALIDATION

Unlike C_{set}, in V_{set} we conducted experiments with mixtures of Bentonite, S1, and S2 at different fractions (Table 2). The V_{set} allows us to verify 1) the size-dependency of SCI functions and 2) whether the SCI functions, derived from C_{set}, are applicable to a broader range of conditions. There are two notes associated with Figure 7. First, results from C_{set} shows that the pairs optical-A_2 provide much less accurate estimations. Hence, optical-A_2 pairs were excluded in this analysis. Second, V_{set} conditions 4 and 5 in Table 2 (or Figures 7d,e), are quite similar due to the uncertainties in controlling the amount of S2 which was partially deposited during the experiments. Nevertheless, V_{set} successfully creates distinctive SPM concentrations with different ratios of Bentonite, S1, and S2.

Figure 7 highlights two groups of the same data population: 1) all optical/acoustic pairs, i.e., the small inset figures and 2) the extractions (zoom in) of the most accurate estimation within ± 10% for both f_{mud} and concentration. In general, SCI-optical functions (filled markers) present in all conditions, confirming that this method is accurate and practical. Another observation is that whether or not SCI functions can reasonably predict f_{mud} depends heavily on the percentage of Bentonite in the mixture. For example, an increase in the absolute amount of coarser sediment leads to decrease in the accuracy of f_{mud} calculation (Fig. 7a'- f'). In mud-dominated environment (Fig. 7a,b,f), SCI-C12 and SCI-C1 functions offer adequate estimations. When the mixture becomes coarser, S2 dominant, as in Figure 7c, the best SCI functions change to SCI-C2-acoustic, i.e., more open markers presented. This is because acoustic sensors capture the changes in sand sizes better than optical sensors do, particularly for sand S2. Similarly, in S1 dominant conditions, Figure 7d,e, SCI-C1 functions have the best performances.

5 DISCUSSION

5.1 Frequency/wavelength and particle size

This section discusses the possibility of applying our proposed method to field measurements where the contents of the SPM are often unknown, e.g., mud/sand fraction in estuaries. V_{set} is a test of schematic mixtures that might be observed in field measurements, offering a much more complicated environment compared with C_{set} from which the SCI-C12 functions were derived. V_{set} provides double the range of concentrations and different ratios of Be, S1, and S2 in comparison to C_{set}. Figure 8 shows the RMSE, indicating how well, the SCI-C12 functions work under bimodal (C1 and C2) and multimodal (V_{set}) particle size distribution environments. Visually, higher acoustic frequencies (>4 MHz) often result in better estimation compared to lower acoustic frequencies (1 and 2 MHz). Regarding V_{set}, SCI-C12 functions correctly reproduce the mud/sand fraction from 8 to 26% of uncertainty with frequencies from 2 to 6 MHz (Fig. 8c).

The applications of SCI-C12-acoustic (Fig. 8d,e,f), however, generate erroneous outcomes (> 100%) except for optical-A_6 pair (Fig. 8f). There are a few notes concerning the performance of the SCI-C12 functions. It is clear that the accuracy declines with the increase of complexity of the mixtures, i.e., from C_{set} to V_{set}. Additionally, instead of 30 data points as in C1 and C2, there are only 6 data points in V_{set} (Table 2). Hence, the weight of one error is exaggerated and somewhat skews the RMSE calculation. The low resolution of sensor O_{700} and A_8 at lower concentrations also plays an important role in reducing the performance of the SCI-functions.

The finding that optical-A_6 pair is one of the best combinations becomes clear when put in the context of scattering theory, i.e., $2\pi r\lambda^{-1} \approx 1$. The optimal particle diameters for acoustic at frequencies 4 and 6 MHz are 120 and 80 μm, respectively. If we calculate a hypothetical mean particle diameter for each condition in V_{set} as $d_{avg} = \sum_i^n d_i p_i$ where d_i is the particle size of size fraction i (Bentonite = 40, S1 = 110, S2 = 240 μm), and p_i is the percentage by mass of size fraction i (Table 2). The results show that the values of d_{avg} vary from 40 to 136 μm which is just around the optimal working ranges of frequencies 4-6 MHz. This might explain why SCI-optical-$A_{4,6}$ functions almost always produce the most accurate predictions in both C_{set} and V_{set}. Application of the same theory helps to explain why lower frequencies, < 2 MHz, sometimes generate errors in prediction by several order of magnitude, because those frequencies are only sensitive to much larger particle sizes. The miscalculation of SCI-optical-A_8 pairs for V_{set}, however, is not easy to explain since the sensor A_8 only provides final output in the form of mass concentration without revealing the inversion function used or the raw signal. The differences between $Ca_{estimated}$ and $C_{measured}$ escalate with the increase of sand size, concentration and complexity degree, i.e., multimodal size distribution, of the suspension. Therefore, one possible conclusion from Figure 7 and 8 is that A_8 sensor does not work properly under multimodal and/or coarser sand particle environments.

In a relatively different pattern, optical sensors are quite consistent and offer much lower variations in f_{mud} and total concentration predictions. Further investigation of coefficient of variations (standard deviation/mean) shows that optical sensors are more sensitive to the change of f_{mud}, while acoustic sensors are more sensitive to the change of particle sizes. For example, a reduction in f_{mud} from 100 to 0% results in an increase in O_{700} signal of 6.1%, but only 0.6% for A_6 signal. In contrast, signal differences between S1 and S2 conditions for O_{700} is almost 4.1%, while for A_6 is ≈ 10%. Thus, the homogeneity or complexity of the mixture are not as important for optical sensors as for acoustic sensors.

5.2 Multi-frequency or multi-wavelength

A question of interest is whether the same procedure is applicable to two paired optical sensors or two paired acoustic sensors of different wavelengths/frequencies. Inversion of multi-frequency acoustic backscatter data to obtain sediment size and concentration profile often requires some prior knowledge of the suspension and a suitable computational algorithm (Moate and Thorne, 2009; Lynch et al., 1994; Thorne and Hurther, 2014; Thorne et al., 2021). The present study does not intend to make comparison between our approach and other existing methods. Rather, we would like to discuss a possible way to take advantage of multi-wavelength and/or multi-frequency measurements to achieve similar results. Figure 9 highlights a few examples of combinations of different wavelengths/frequencies. While no useful information could be extracted from optical-optical pairs (Fig. 9), the relationship between multi-frequency measurements is very promising, alike Figure 4c,d. For example, in Figure 9a-c, pure Bentonite and pure sand conditions are still set a clear boundaries for all other intermediate ratios of mud/sand. A certain slope/intercept associated with each condition also holds for a specific mud/sand ratio. Differences between finer and coarser sand particle sizes are seen in some cases (Fig. 9a,b,c). Nevertheless, providing a full calculation for SCI-acoustic-acoustic functions is out of the scope of this study. In future, this approach will be further investigated.

6 CONCLUSIONS

This study proposes a new approach to obtain mud/sand fraction and the total concentration of a suspension based on conjugating optical-acoustic measurements. Two sets of experiments, providing bimodal (C_{set}) and multimodal (V_{set}) particle size distributions, are used to calibrate and validate our SCI functions. In general, SCI-optical functions have a better performance than their counterpart SCI-acoustic functions. The results show that for suspension in which the particle size is known (e.g., SCI functions were chosen accordingly) predicted concentrations can be as accurate as $\approx 7\ mg/L$ (Fig. 6). Without prior knowledge of particle sizes, SCI functions derived from C12 can be applied to various sediment mixtures with a reasonable error, i.e., < 10% for f_{mud} and < 15% for concentration. For example, considering there is an average size for each condition in V_{set} the best optical-acoustic pairs are optical wavelength 620-700 nm and acoustic frequency 4-6 MHz. The results suggest that the SCI method is highly applicable to sedimentary-dynamic environments, e.g., estuaries and coastal zones, even without sensor calibrations and knowledge of mud/sand ratio. In the near future, the possibility of applying the same approach to multi-frequency acoustic measurements and a larger range of concentrations as well as different types of minerals and particle sizes will be investigated.

7 ACKNOWLEDGEMENT

This work was co-funded by Ifremer and the PHRESQUES project, coordinated by the GIP Seine Aval. PHRESQUES was funded by the CPIER «Vallée de Seine», the Seine Normandy Water Agency (AESN), and the Normandie and Ile de France Regions. This project is also supported by the eLTER «Zone Atelier Seine». We are also grateful for the critiques provided by Michael Fettweis during the preparation of this manuscript.

C	Bentonite/sand fraction (f_{mud}) [%]			Task	Time
[mg/L]	100	75, 50, 25	0		[min]
15	(pure mud)	(mixed mud/sand)	(pure sand)	1. Bentonite stabilized in a beaker	0-30
25				2. Bentonite stabilized in DEXMES	30-60
50	C1_100	C1_75,50,25	C1_0	3. Introduce sand in DEXMES	55
100	or	or	or	4. Data recording	60-70
150	C2_100	C2_75,50,25	C2_0	5. Water sampling	71-73
200				6. New sediment for the next step	Repeat task 1-5

Table 1: Experimental conditions and procedure of the calibration set, C_{set}. S1: sand particle size d_{50} = 110 μm. S2: sand particle size d_{50} = 240 μm.

Run	C	Bentonite/sand fraction [%]			d_{avg}
	[mg/L]	Be	S1 (110 μm)	S2 (240 μm)	[μm]
1	50 (46)	100 (100)	0 (0)	0 (0)	40
2	75 (68)	67 (67)	33 (33)	0 (0)	63
3	125 (103)	40 (44)	20 (21)	40 (35)	125
4	200 (174)	25 (26)	50 (54)	25 (20)	118
5	250 (191)	20 (23)	40 (45)	40 (32)	136
6	400 (330)	50 (54)	25 (31)	25 (15)	92

Table 2: Experimental conditions and procedure of the validation set, V_{set}. x (y): target (measured). $d_{avg} = \sum_i^n d_i p_i$ where d_i is the particle size of size fraction i, and p_i is the percentage by mass of size fraction i. i denotes S1 and S2.

	Sensor	Working frequency [MHz] / wavelength [nm]	Sampling frequency [Hz]	Data output unit	Notation in text
Acoustic	LISST-ABS	8	1	mg/L	A_8
	ADV Vector	6	32	SNR - dB	A_6
	AQUAscat 1000R (Transducer 4 MHz)	4	32	count	A_4
	AQUAscat 1000R (Transducer 2 MHz)	2	32	count	A_2
	AQUAscat 1000R (Transducer 1 MHz)	1	32	count	A_1
	AQUAscat 1000R (Transducer 0.5 MHz)	0.5	32	count	$A_{0.5}$
Optical	HydroScat-4 (Channel 4)	852	1	m^{-1}	O_{852}
	Wetlabs_FLNTU	700	1	count -> NTU	O_{700}
	HydroScat-4 (Channel 3)	620	1	m^{-1}	O_{620}
	HydroScat-4 (Channel 2)	532	1	m^{-1}	O_{532}
	HydroScat-4 (Channel 1)	420	1	m^{-1}	O_{420}

Table 3: A summary of working conditions of all sensors used in this study. Data from LISST-100X (not shown here) is used to verify the particle size distribution in suspension, but is not paired with other sensors during the data analysis process.

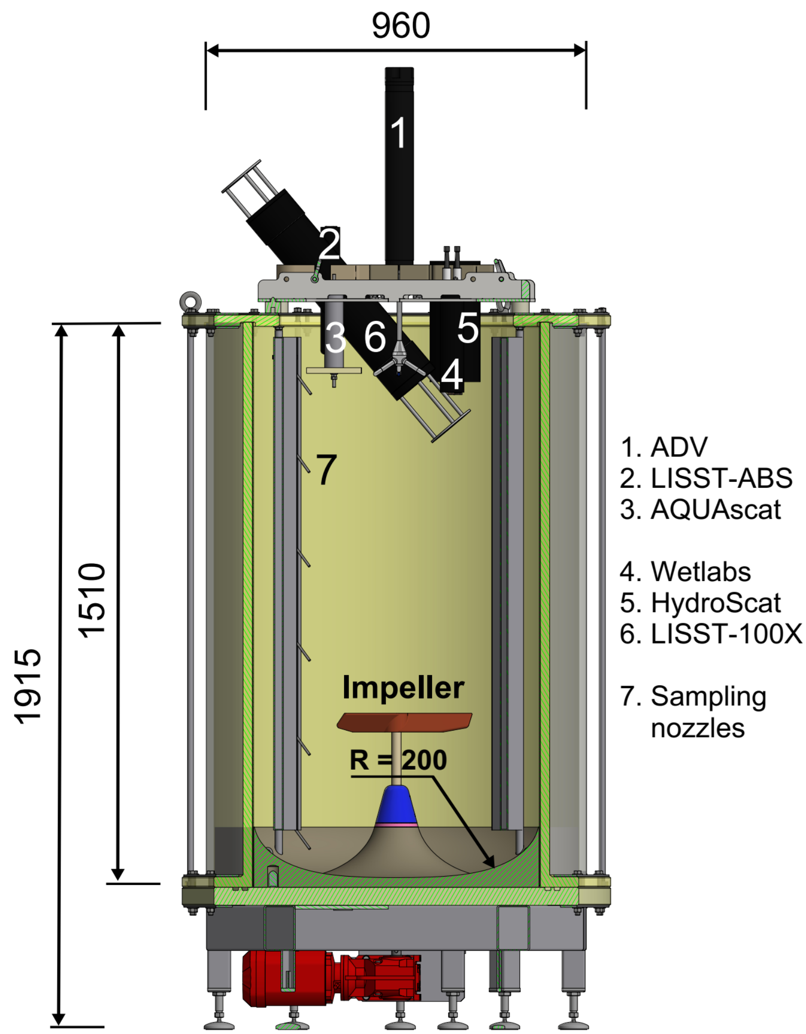

Figure 1: Experimental setup of the DEXMES tank (not to scale). Measuring volumes of all sensors were set at similar level as of water sampling nozzle, ≈ 25-26 cm below the water surface.

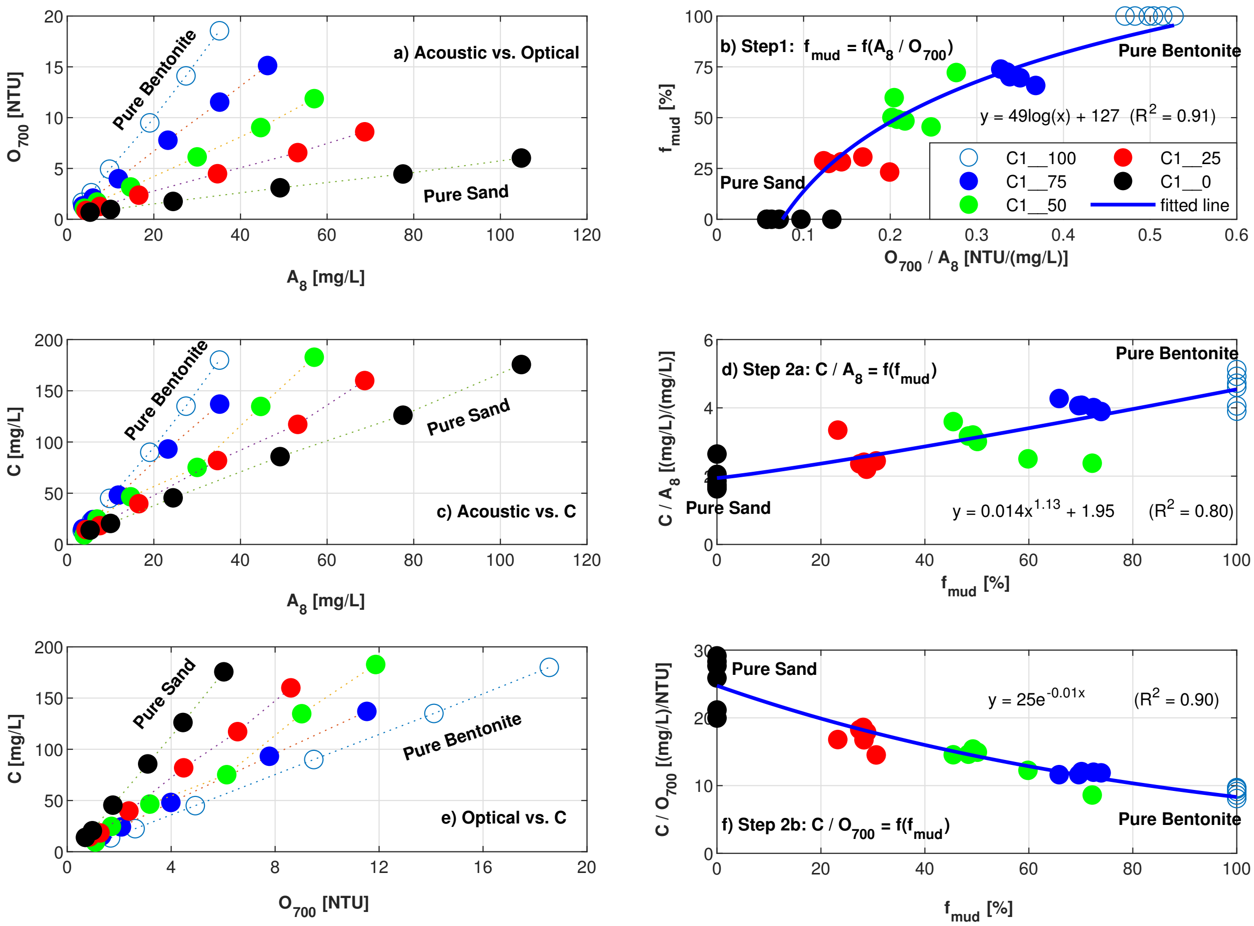

Figure 2: An example of relationships between O_{700} and A_8 (Optical 700 nm and Acoustic 8 MHz) and total concentrations. Only Calibration set for sand S1 (C1) data were used in this demonstration. Step 1, 2a, 2b: please refer to equations 1, 2, and 3.

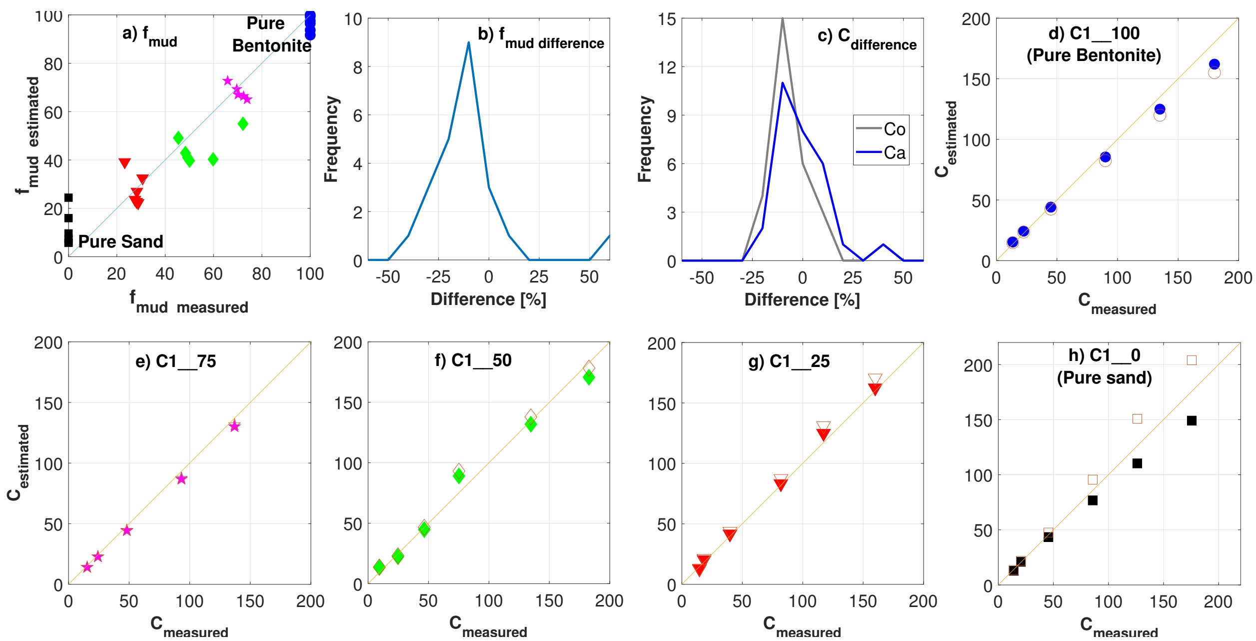

Figure 3: Differences between estimated and measured of f_{mud} and total concentration for the pair O_{700}, A_8. Ca: empty markers. Co: filled markers.

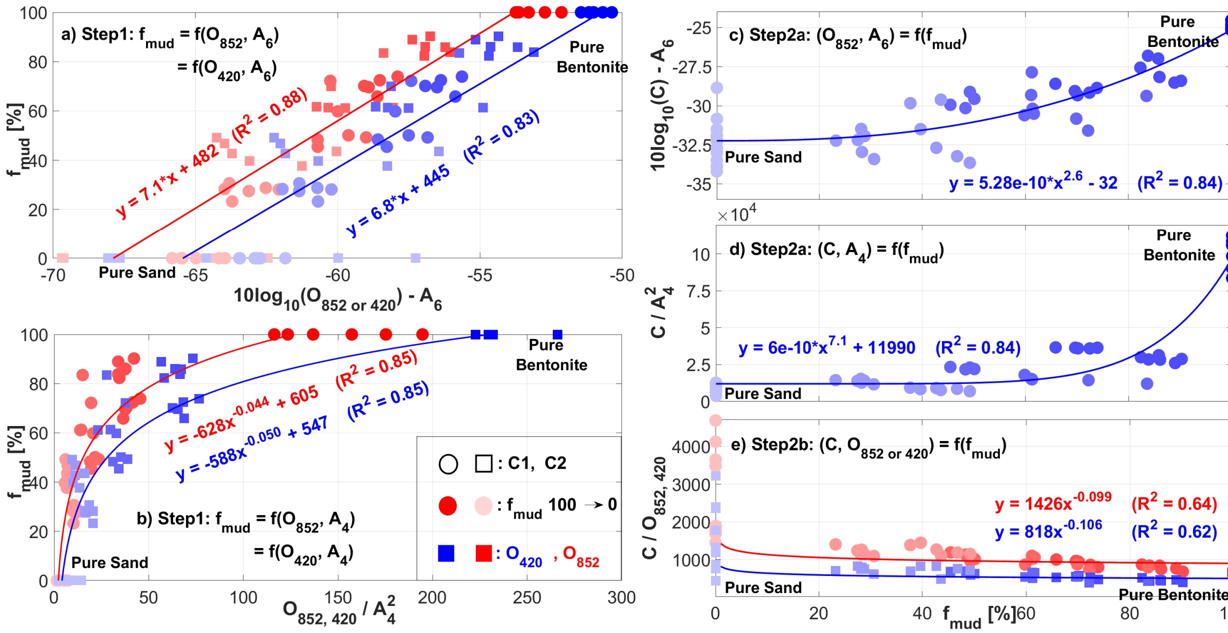

Figure 4: Application of SCI method to four optical/acoustic pairs with all data in Cset (C12). The reductions of f_{mud} from 100% to 0% are shown by the darkest color to lightest color. Blue: data from O_{420}. Red: data from O_{852}. The displayed functions are obtained from data set C12.

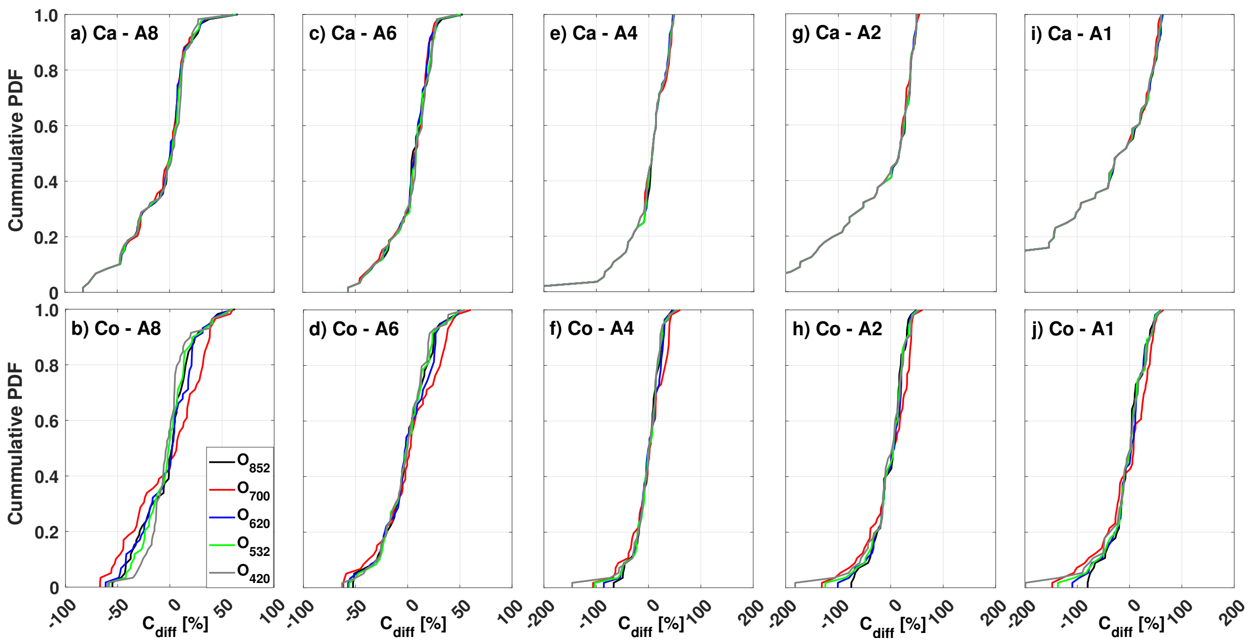

Figure 5: Comparison of all pairs when applying SCI-C12 functions to estimate Ca (step 2a) and Co (step 2b). Concentration differences, in %, between C$_{measured}$ and Ca, Co. $C_{diff} = \frac{(C_{measured} - C_{estimated})}{C_{measured}} 100\%$.

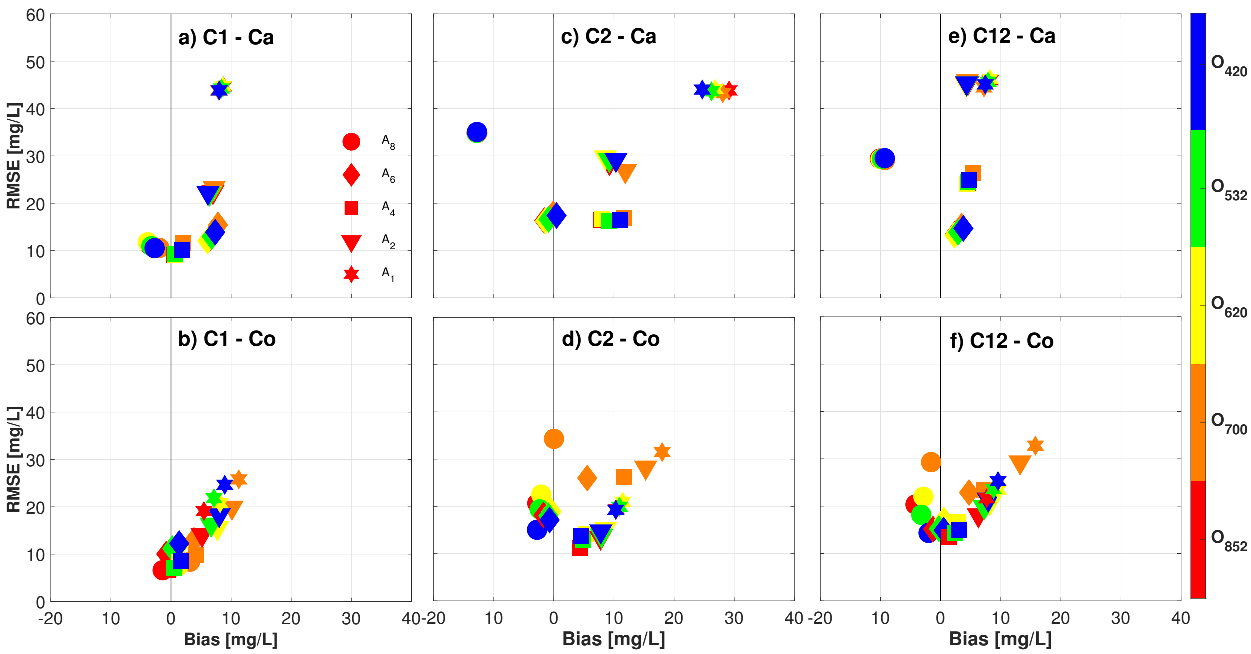

Figure 6: Comparison of the performances of different SCI functions obtained from different data sets, i.e., C1 (a, b), C2 (c, d) or C12 (e, f). RMSE and bias of each pair. Bias = $\frac{\sum(C_{measured}-C_{estimated})}{m}$. RMSE = $\sqrt{\overline{(C_{measured}-C_{estimated})^2}}$, where m is the number of data points.

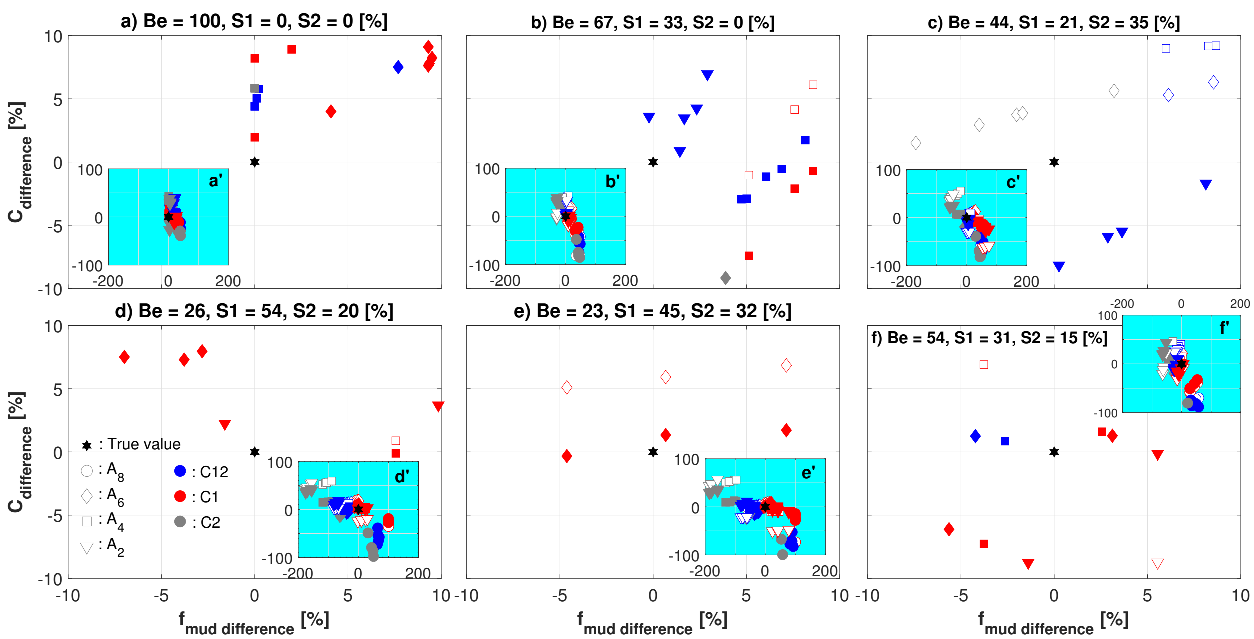

Figure 7: Application of SCI functions, derived from C_{set}, to V_{set} data. The sub-figures show all optical/acoustic pairs that predict f_{mud} and concentration within ± 10% error. The small inset inside each sub-figure shows results from all pairs of each experimental condition. The legend should be read as a combination of marker + color + filled/open. Where filled marker = Co, empty marker = Ca. For example, a blue-filled-diamond means Co was obtained by C12-($O_{800->420}-A_6$) functions.

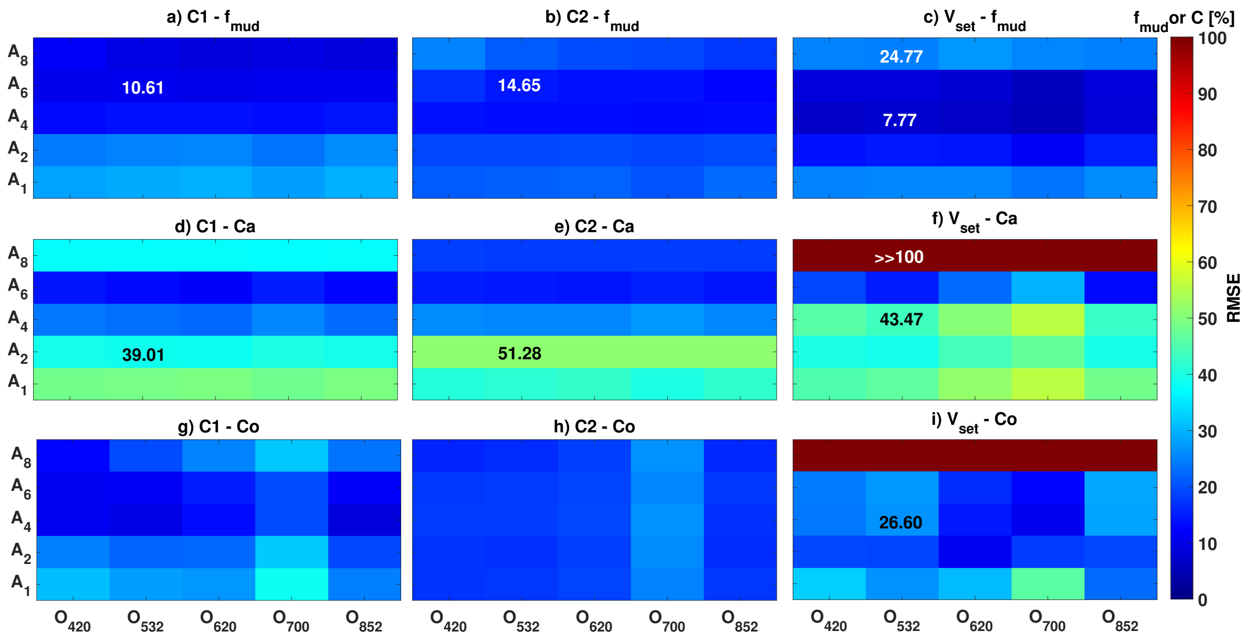

Figure 8: RMSE of the application of SCI-C12 functions to data sets C1, C2, and V_{set}. RMSE = $\sqrt{(X_{measured} - X_{estimated})^2}$, where $X = f_{mud}$ or concentration. A few numbers associated with specific color are also given for better references. In this figure, SCI functions derived from data set C12 were applied to calculate Ca (step 2a) and Co (step 2b) of different data sets, i.e., from bimodal to multimodal particle size mixtures.

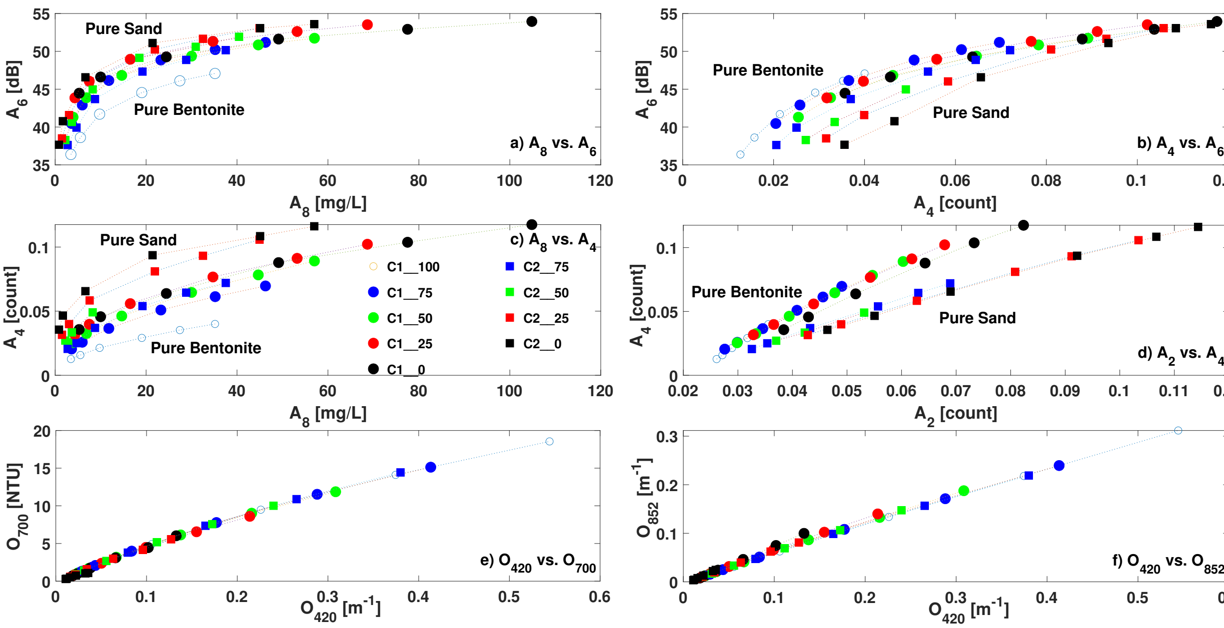

Figure 9: Examples of combinations of acoustic-acoustic, and optical-optical pairs. The two upper panels show similar pattern as seen in Figure 2, indicating that it is possible to derive a similar SCI functions from acoustic-acoustic data set, i.e., sub-figures a, b, c. All signals are raw, uncalibrated.

A APPENDIX A. SCI FUNCTIONS - A FURTHER DISCUSSION

In Section 3.1 we proposed to derive the SCI functions based on searching for the "optimal" functions, i.e., functions that have the highest R^2. Fundamentally, equations 2 and 3 should be able to combine into one equation in which optical and acoustic terms represent the mud and sand fractions, respectively. Figures 2a,c,e show that all conditions converge to point (0,0). Hence, the relationship between f_{mud} and ratio of O_{700}/A_8 should have a linear form of $y = a*x$, as do the relationships between C and O_{700} and between C and A_8. The SCI functions – Equations 1, 2, and 3 – then can be written as:

$$f_{mud} = t*(O_{700}/A_8) \tag{A.1}$$

$$Concentration = m*f_{mud}*O_{700} + n*(100 - f_{mud})*A_8 \tag{A.2}$$

where t, m, and n are constants. Fitting data from Figure 2 to equations A.1 and A.2 gives t = 200, m = 0.1 and n = 0.02. SCI functions written in the form of A.2 provide results that are very similar to equations 1 and 3. However, there are two primary drawbacks using equations A.1 and A.2. First, mud or sand reflects both optical and acoustic signals to different degrees. For example, the amount of sand needed to increase the optical signal by 10 NTU might be several times the amount of mud. On the contrary, the amount of mud needed to increase the acoustic singal by 5 dB might take several times the amount of sand. To date, the percentages of backscatter signals reflected by mud and by sand in a mixed suspension are not fully understood. Hence, mathematical expression of such behaviors is rather difficult, particularly in case of AQUAscat and ADV where the relationships are not linear. Second, the resolutions of the sensors used in these experiments are not high enough to differentiate between small increases in each concentration step and/or f_{mud}, e.g., from concentrations of 150 mg/L to 200 mg/L. Subsequently, derivations of coefficients such as t, m, and n are not necessarily better than using empirical functions as shown in the main document.

B APPENDIX B. SCI FUNCTIONS - ALL PAIRS

This section provides the SCI functions of all the other pairs. In these figures, blue circles or red squares represent data from C1 or C2, respectively. Blue or red curves indicate the SCI functions obtained from either C1 or C2 data set. The mathematical functions displayed in the sub-figures were obtained from data set C12 (black line). As discussed in Section 3.2, for pure Bentonite and pure sand conditions only concentration C = 100 mg/L was used to minimized the variations in these two extreme cases.

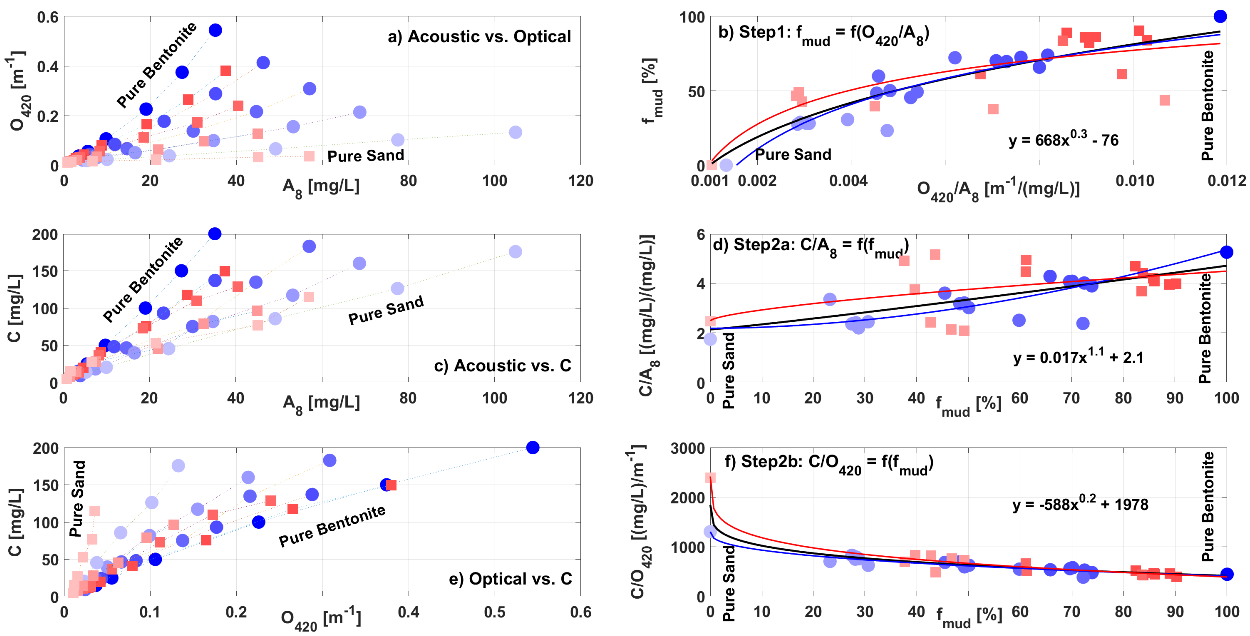

Figure B1: Application of SCI method to the optical/acoustic pair of $\mathbf{O}_{420}$ and $\mathbf{A}_8$ with data in C1 (blue), C2 (red) and C12 (black). The reductions of f_{mud} from 100% to 0% are shown by the darkest color to lightest color. The displayed function are obtained from data set C12.

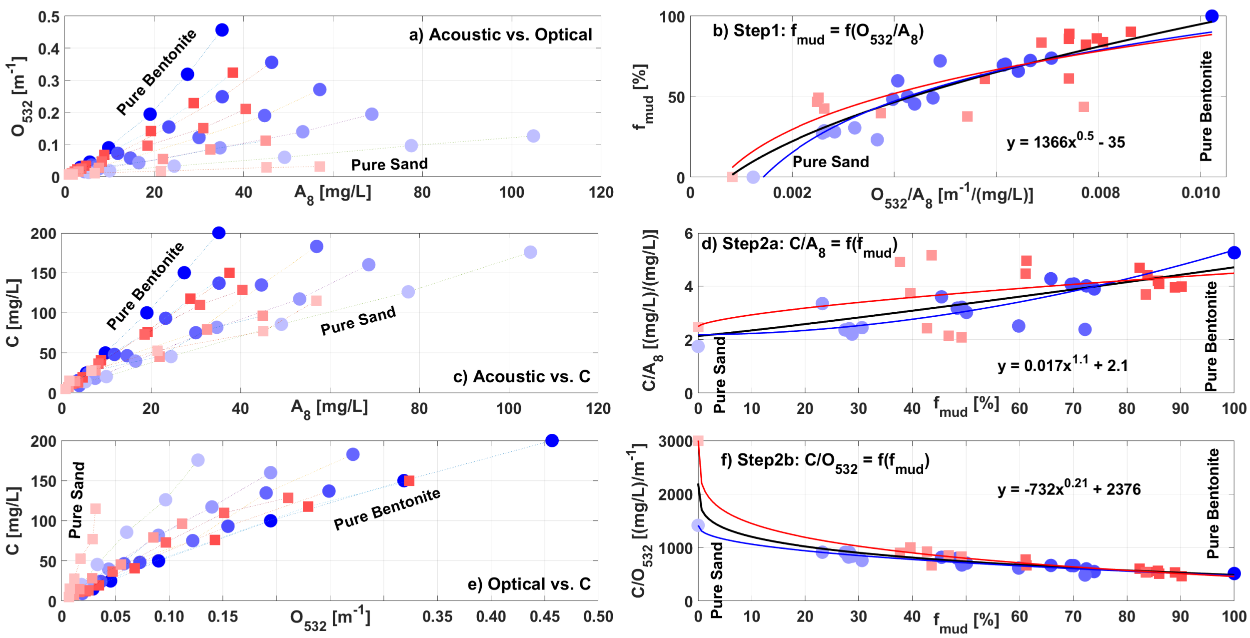

Figure B2: Application of SCI method to the optical/acoustic pair of $\mathbf{O}_{532}$ and $\mathbf{A}_8$ with data in C1 (blue), C2 (red) and C12 (black). The reductions of f_{mud} from 100% to 0% are shown by the darkest color to lightest color. The displayed function are obtained from data set C12.

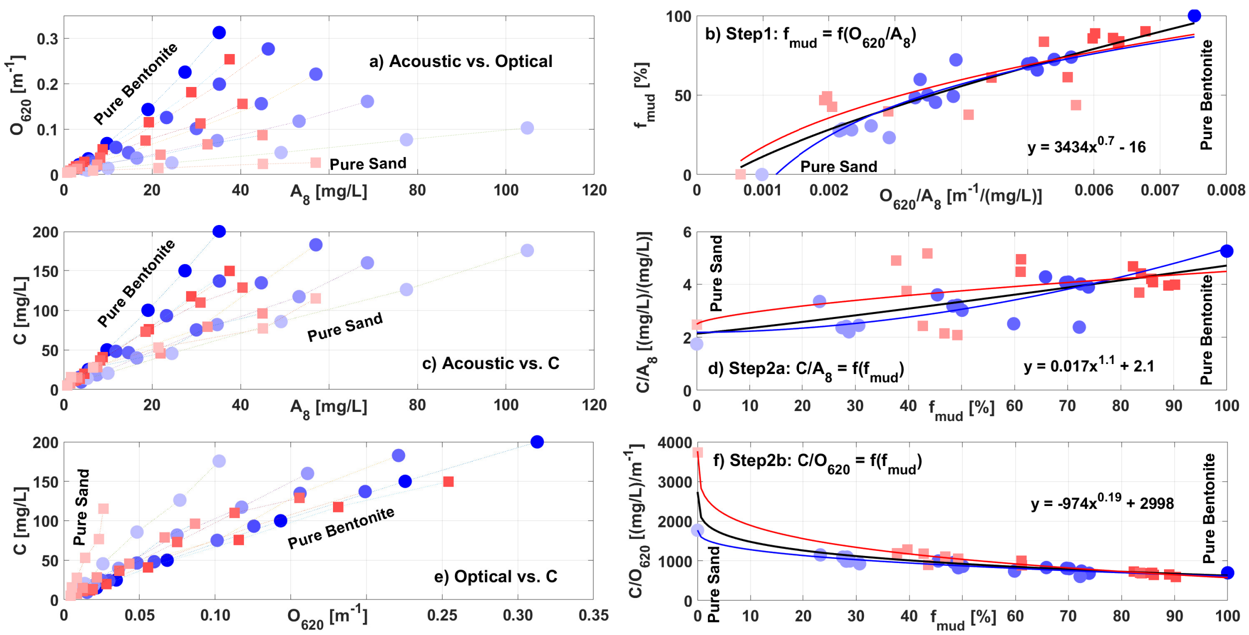

Figure B3: Application of SCI method to the optical/acoustic pair of $\mathbf{O}_{620}$ and $\mathbf{A}_8$ with data in C1 (blue), C2 (red) and C12 (black). The reductions of f_{mud} from 100% to 0% are shown by the darkest color to lightest color. The displayed function are obtained from data set C12.

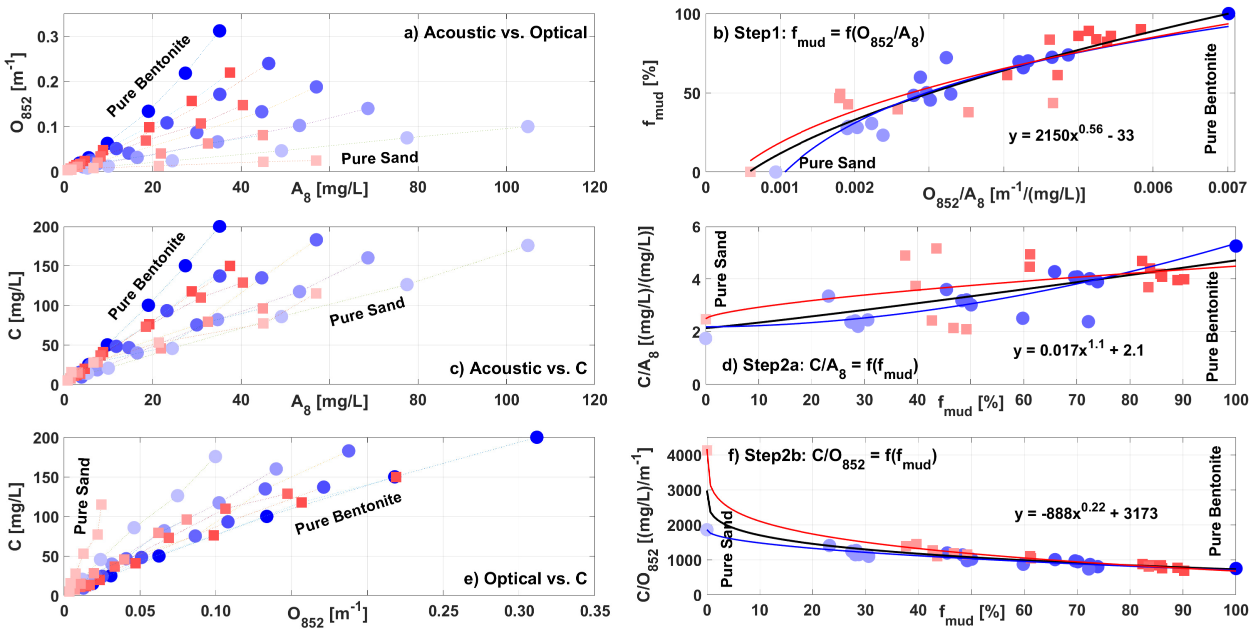

Figure B4: Application of SCI method to the optical/acoustic pair of $\mathbf{O}_{852}$ and $\mathbf{A}_8$ with data in C1 (blue), C2 (red) and C12 (black). The reductions of f_{mud} from 100% to 0% are shown by the darkest color to lightest color. The displayed function are obtained from data set C12.

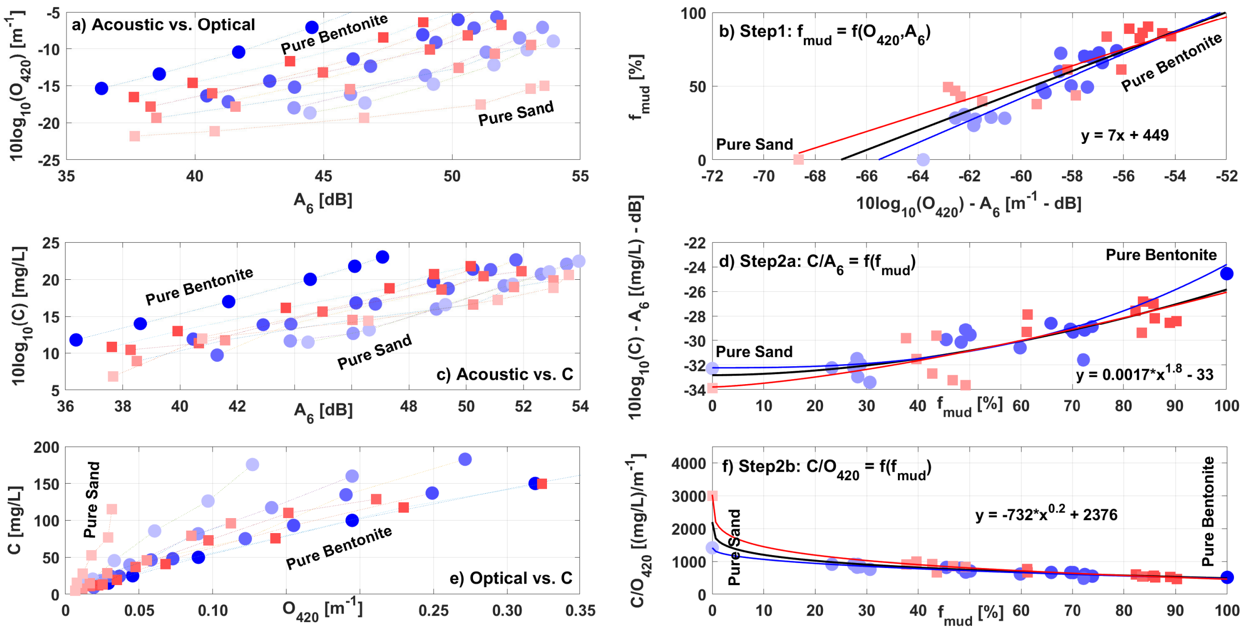

Figure B5: Application of SCI method to the optical/acoustic pair of $\mathbf{O}_{420}$ and $\mathbf{A}_6$ with data in C1 (blue), C2 (red) and C12 (black). The reductions of f_{mud} from 100% to 0% are shown by the darkest color to lightest color. The displayed function are obtained from data set C12.

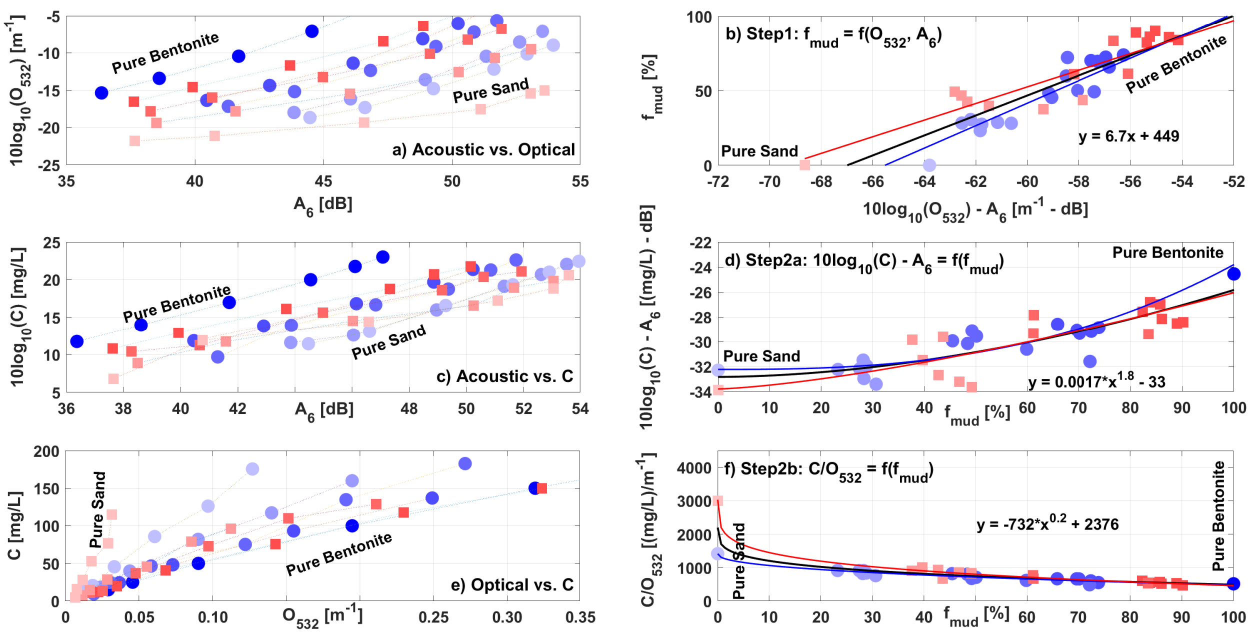

Figure B6: Application of SCI method to the optical/acoustic pair of $\mathbf{O}_{532}$ and $\mathbf{A}_6$ with data in C1 (blue), C2 (red) and C12 (black). The reductions of f_{mud} from 100% to 0% are shown by the darkest color to lightest color. The displayed function are obtained from data set C12.

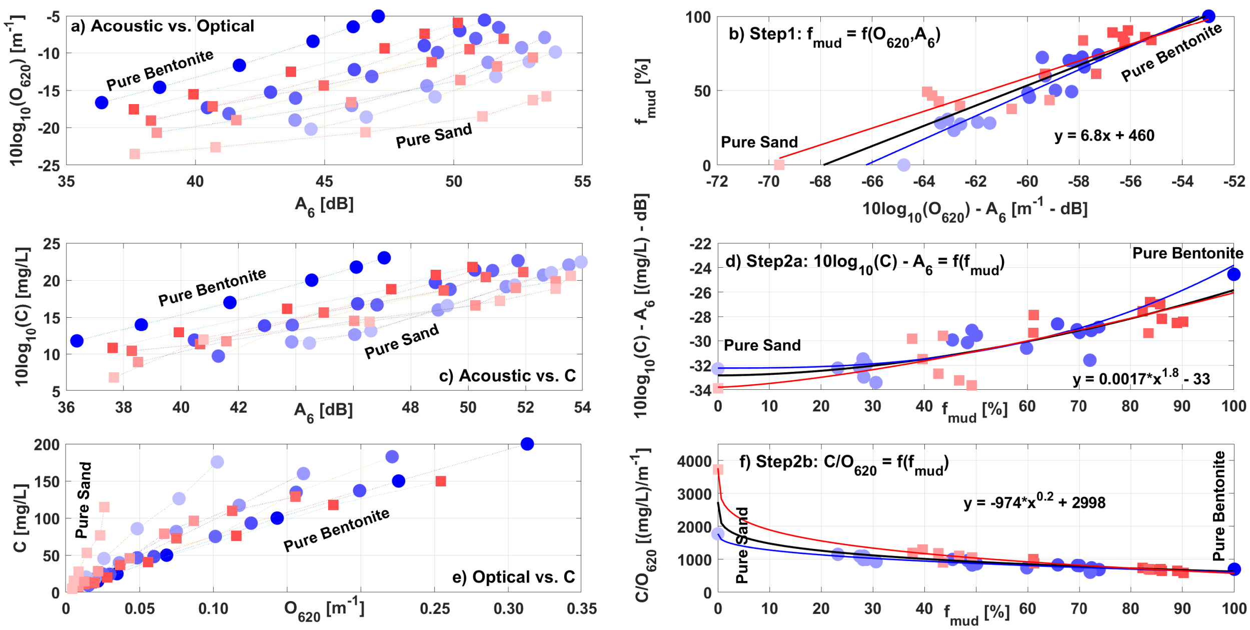

Figure B7: Application of SCI method to the optical/acoustic pair of $\mathbf{O}_{620}$ and $\mathbf{A}_6$ with data in C1 (blue), C2 (red) and C12 (black). The reductions of f_{mud} from 100% to 0% are shown by the darkest color to lightest color. The displayed function are obtained from data set C12.

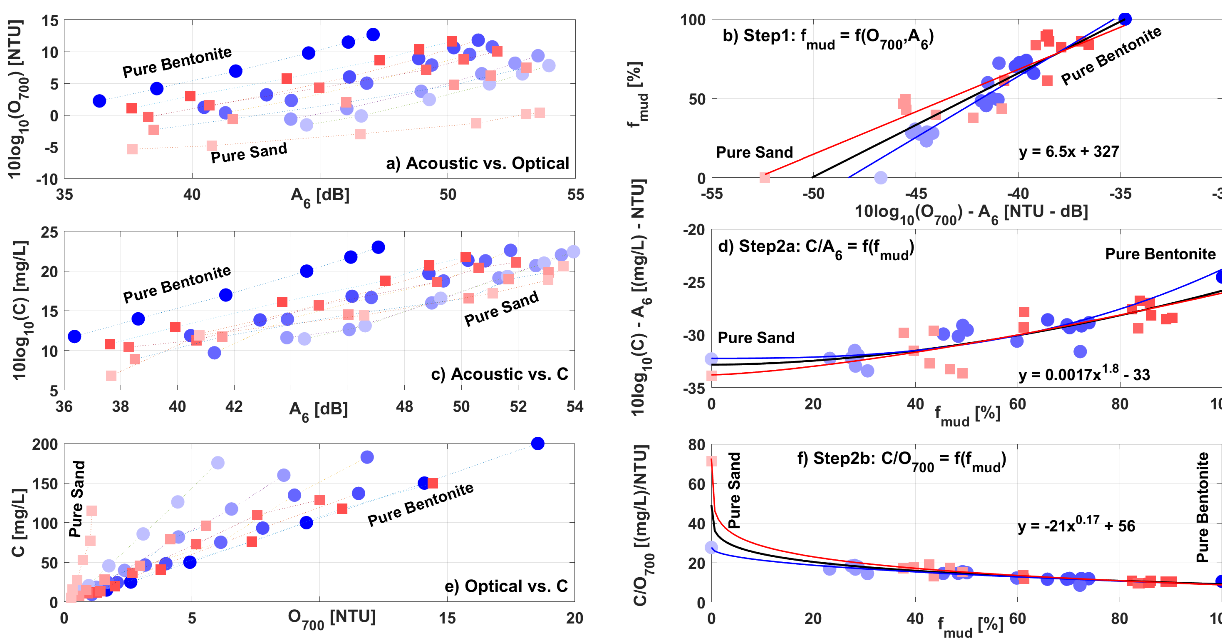

Figure B8: Application of SCI method to the optical/acoustic pair of $\mathbf{O}_{700}$ and $\mathbf{A}_6$ with data in C1 (blue), C2 (red) and C12 (black). The reductions of f_{mud} from 100% to 0% are shown by the darkest color to lightest color. The displayed function are obtained from data set C12.

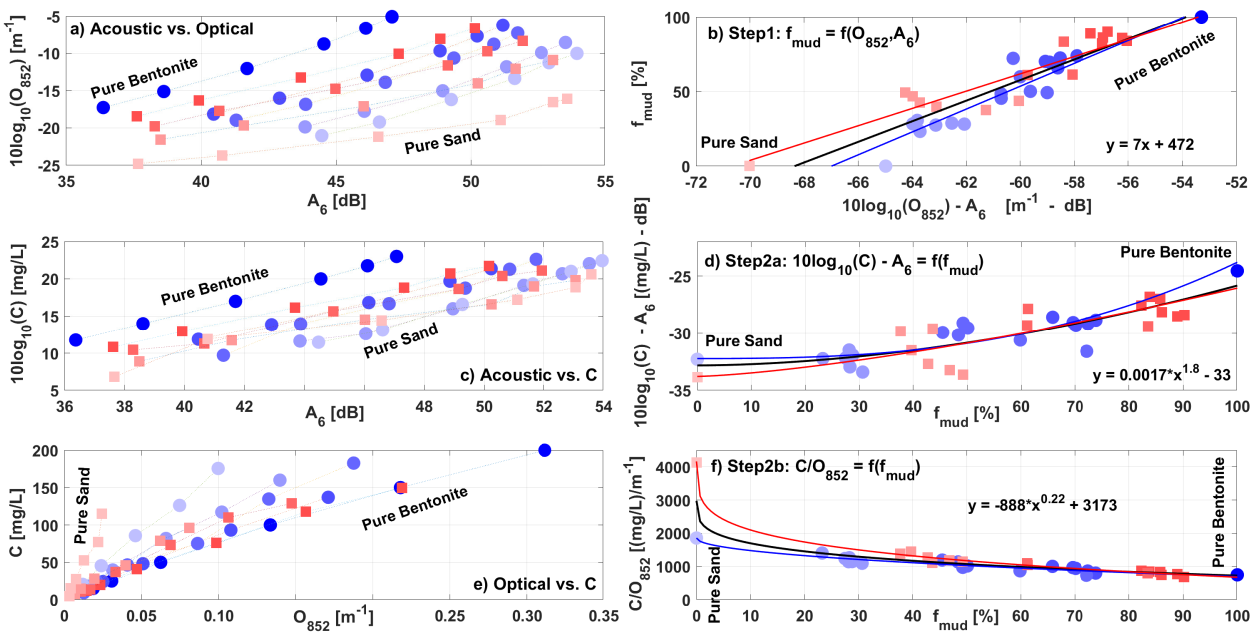

Figure B9: Application of SCI method to the optical/acoustic pair of $\mathbf{O}_{852}$ and $\mathbf{A}_6$ with data in C1 (blue), C2 (red) and C12 (black). The reductions of f_{mud} from 100% to 0% are shown by the darkest color to lightest color. The displayed function are obtained from data set C12.

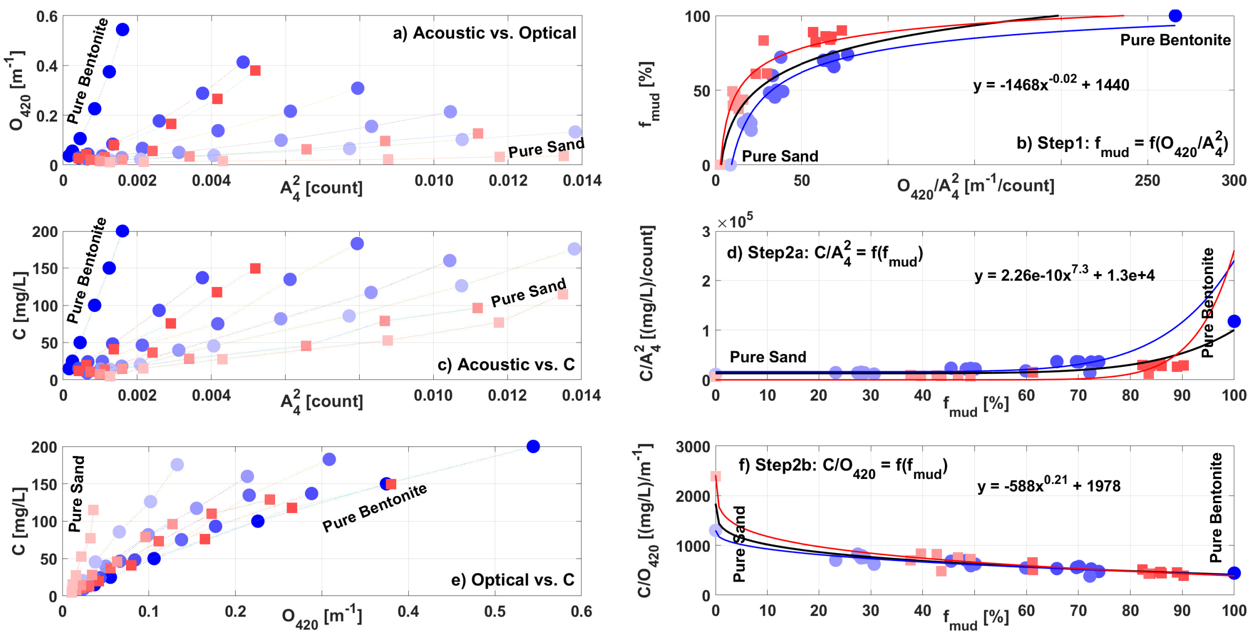

Figure B10: Application of SCI method to the optical/acoustic pair of $\mathbf{O}_{420}$ and $\mathbf{A}_4$ with data in C1 (blue), C2 (red) and C12 (black). The reductions of f_{mud} from 100% to 0% are shown by the darkest color to lightest color. The displayed function are obtained from data set C12.

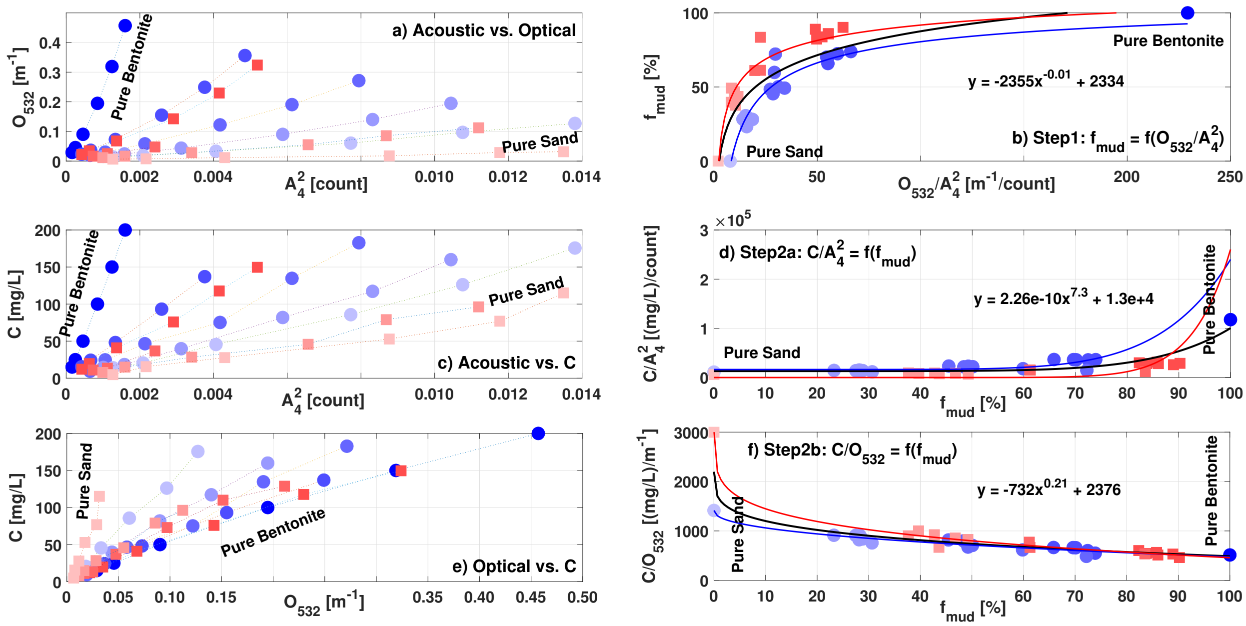

Figure B11: Application of SCI method to the optical/acoustic pair of $\mathbf{O}_{532}$ and $\mathbf{A}_4$ with data in C1 (blue), C2 (red) and C12 (black). The reductions of f_{mud} from 100% to 0% are shown by the darkest color to lightest color. The displayed function are obtained from data set C12.

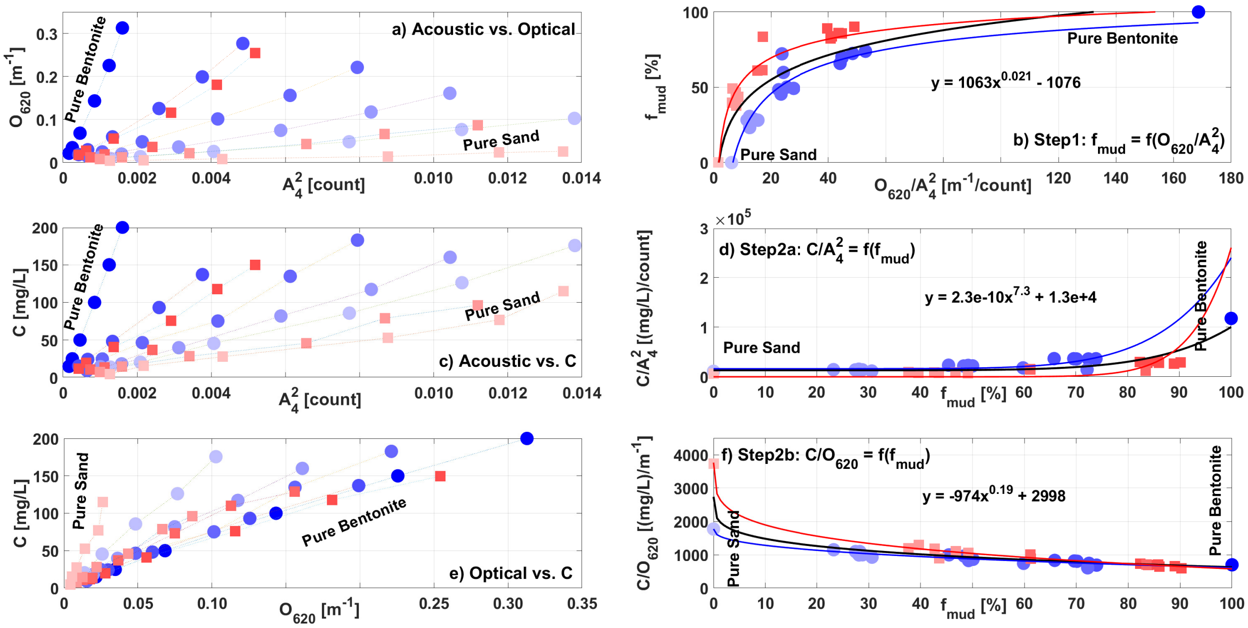

Figure B12: Application of SCI method to the optical/acoustic pair of $\mathbf{O}_{620}$ and $\mathbf{A}_4$ with data in C1 (blue), C2 (red) and C12 (black). The reductions of f_{mud} from 100% to 0% are shown by the darkest color to lightest color. The displayed function are obtained from data set C12.

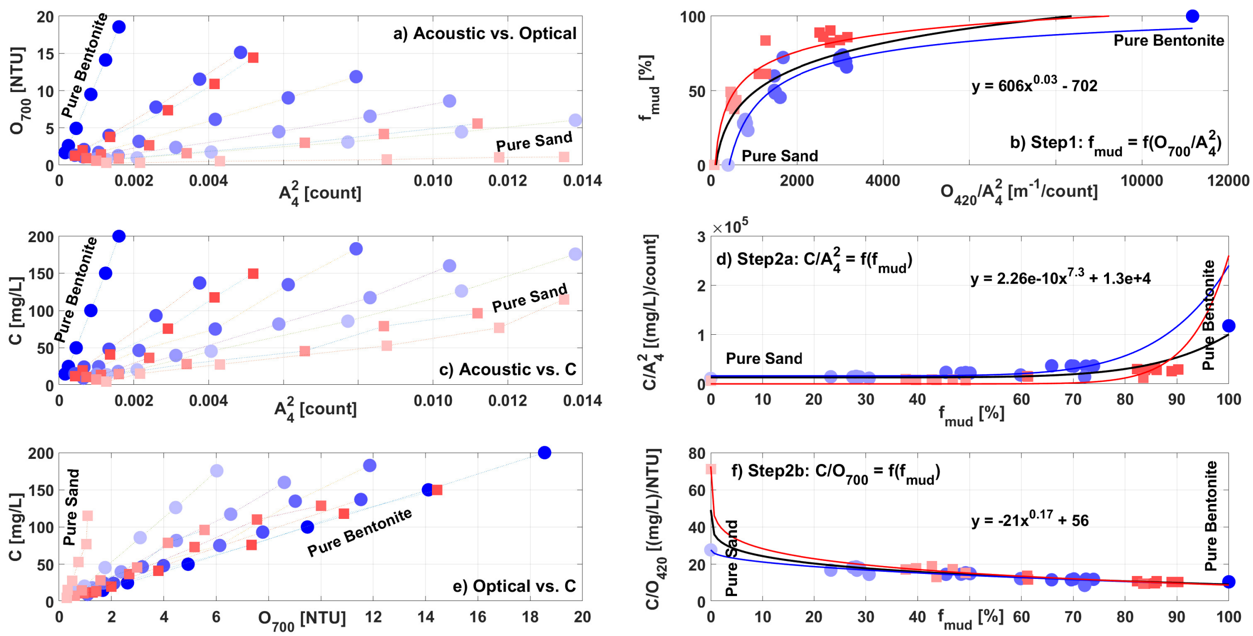

Figure B13: Application of SCI method to the optical/acoustic pair of $\mathbf{O}_{700}$ and $\mathbf{A}_4$ with data in C1 (blue), C2 (red) and C12 (black). The reductions of f_{mud} from 100% to 0% are shown by the darkest color to lightest color. The displayed function are obtained from data set C12.

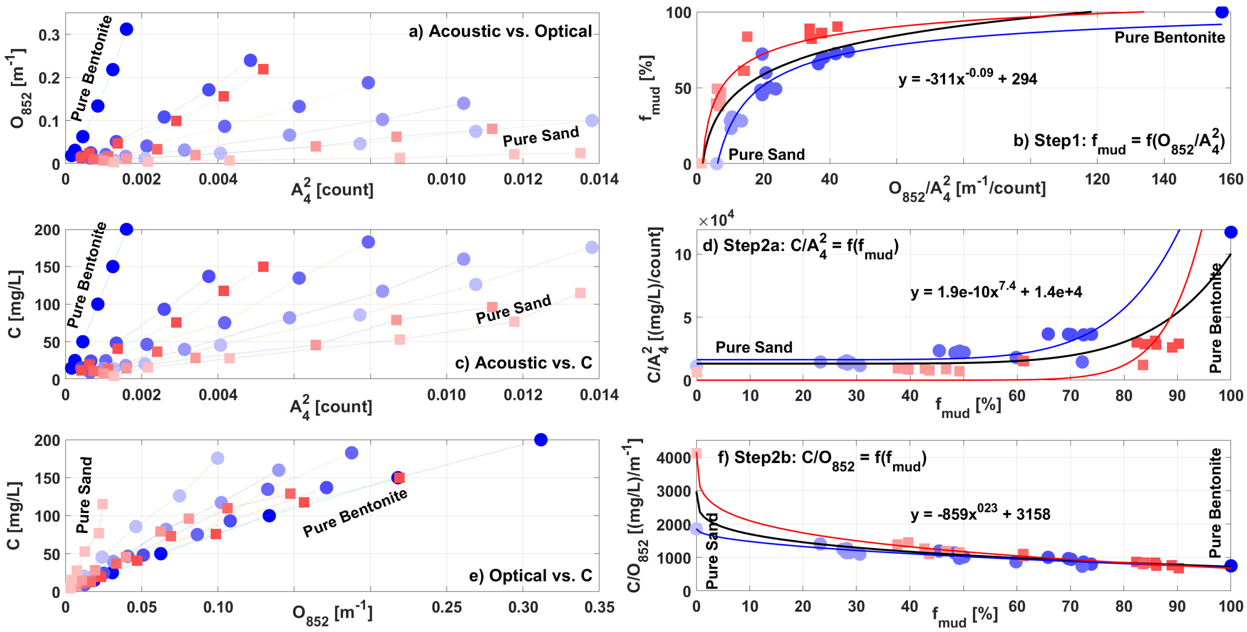

Figure B14: Application of SCI method to the optical/acoustic pair of $\mathbf{O}_{852}$ and $\mathbf{A}_4$ with data in C1 (blue), C2 (red) and C12 (black). The reductions of f_{mud} from 100% to 0% are shown by the darkest color to lightest color. The displayed function are obtained from data set C12.

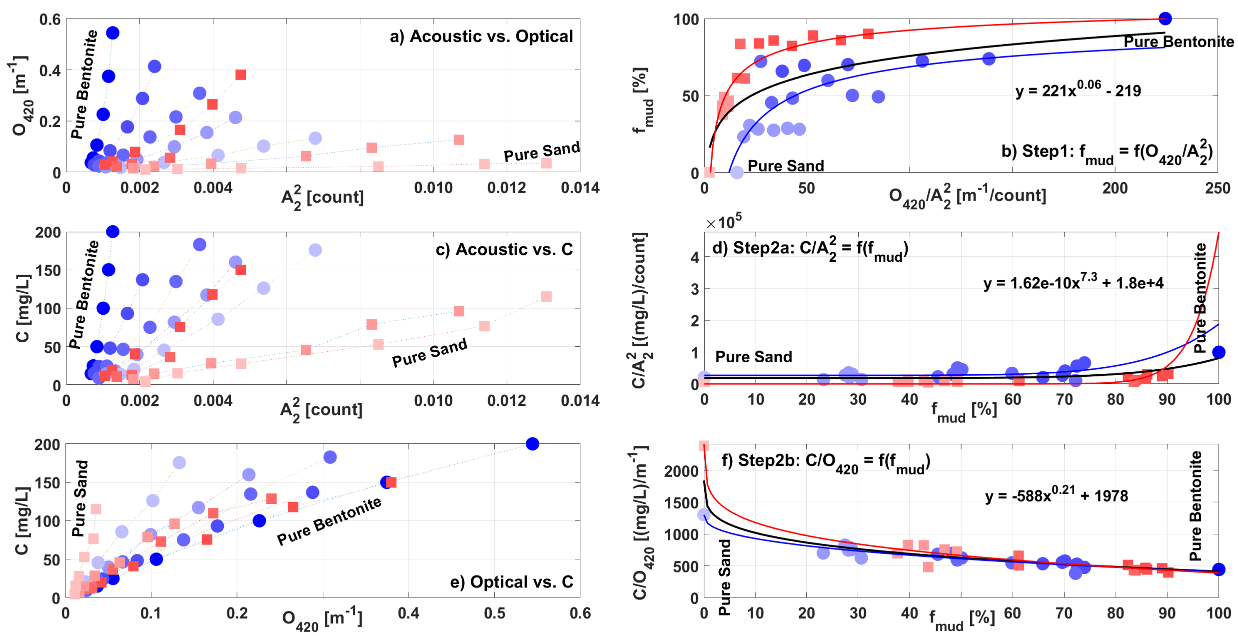

Figure B15: Application of SCI method to the optical/acoustic pair of $\mathbf{O}_{420}$ and $\mathbf{A}_2$ with data in C1 (blue), C2 (red) and C12 (black). The reductions of f_{mud} from 100% to 0% are shown by the darkest color to lightest color. The displayed function are obtained from data set C12.

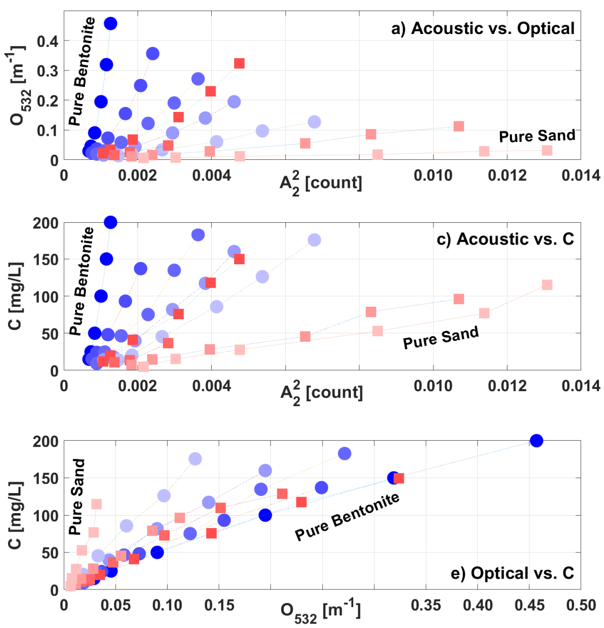

Figure B16: Application of SCI method to the optical/acoustic pair of $\mathbf{O}_{532}$ and $\mathbf{A}_2$ with data in C1 (blue), C2 (red) and C12 (black). The reductions of f_{mud} from 100% to 0% are shown by the darkest color to lightest color. The displayed function are obtained from data set C12.

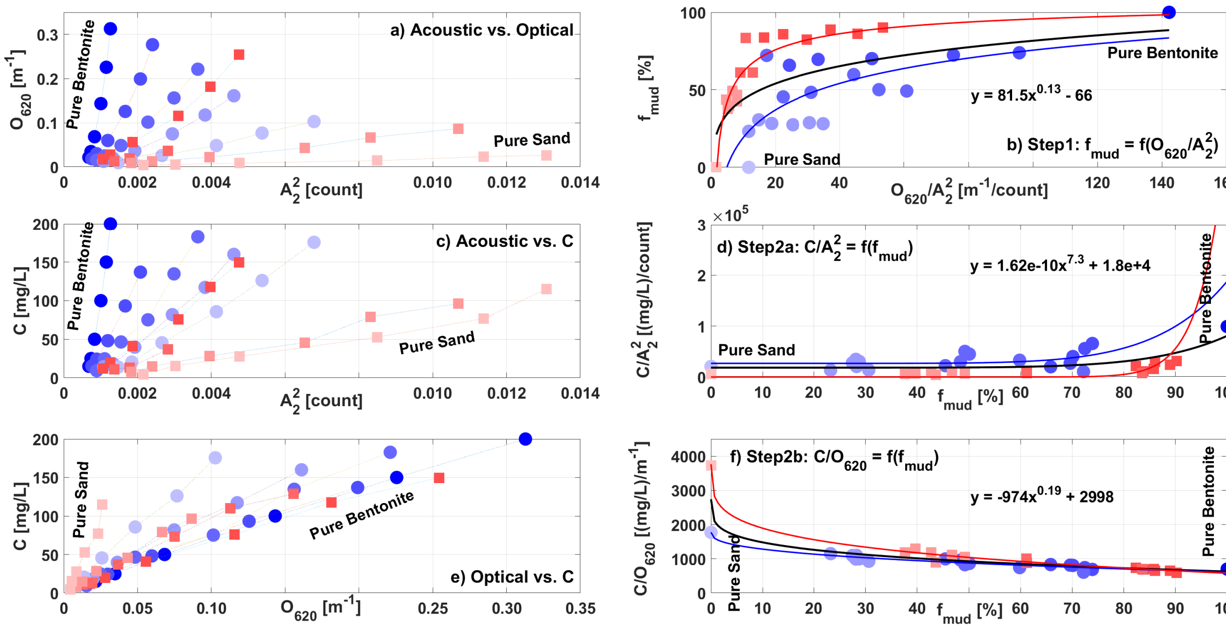

Figure B17: Application of SCI method to the optical/acoustic pair of $\mathbf{O}_{620}$ and $\mathbf{A}_2$ with data in C1 (blue), C2 (red) and C12 (black). The reductions of f_{mud} from 100% to 0% are shown by the darkest color to lightest color. The displayed function are obtained from data set C12.

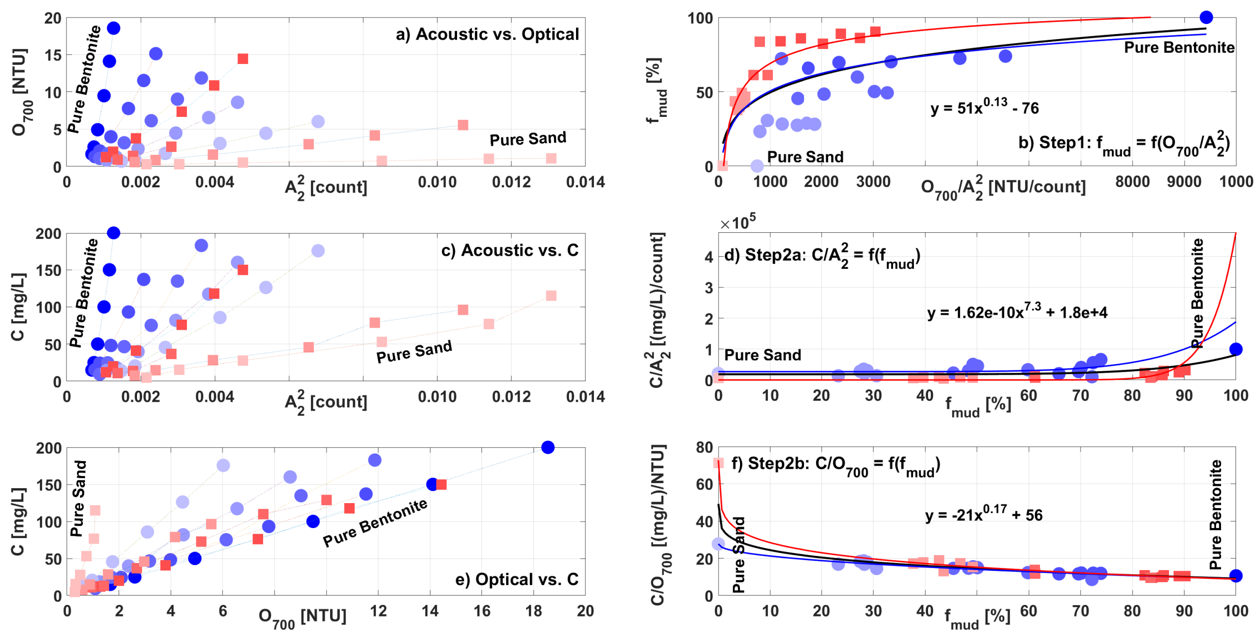

Figure B18: Application of SCI method to the optical/acoustic pair of $\mathbf{O}_{700}$ and $\mathbf{A}_2$ with data in C1 (blue), C2 (red) and C12 (black). The reductions of f_{mud} from 100% to 0% are shown by the darkest color to lightest color. The displayed function are obtained from data set C12.

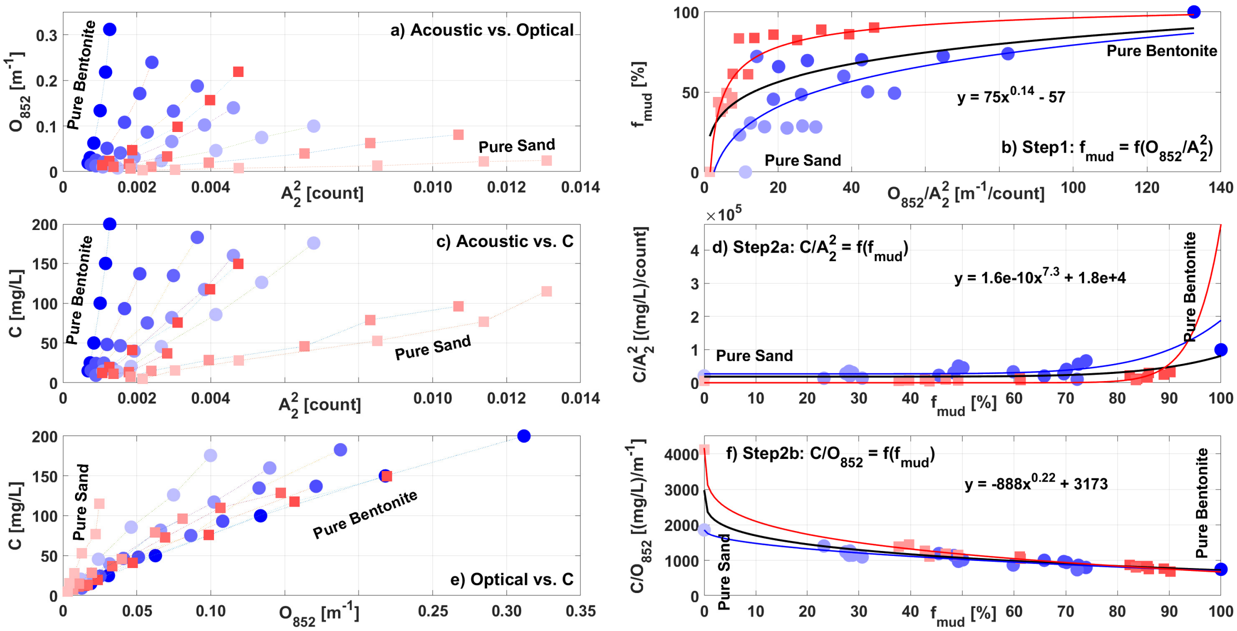

Figure B19: Application of SCI method to the optical/acoustic pair of $\mathbf{O}_{852}$ and $\mathbf{A}_2$ with data in C1 (blue), C2 (red) and C12 (black). The reductions of f_{mud} from 100% to 0% are shown by the darkest color to lightest color. The displayed function are obtained from data set C12.

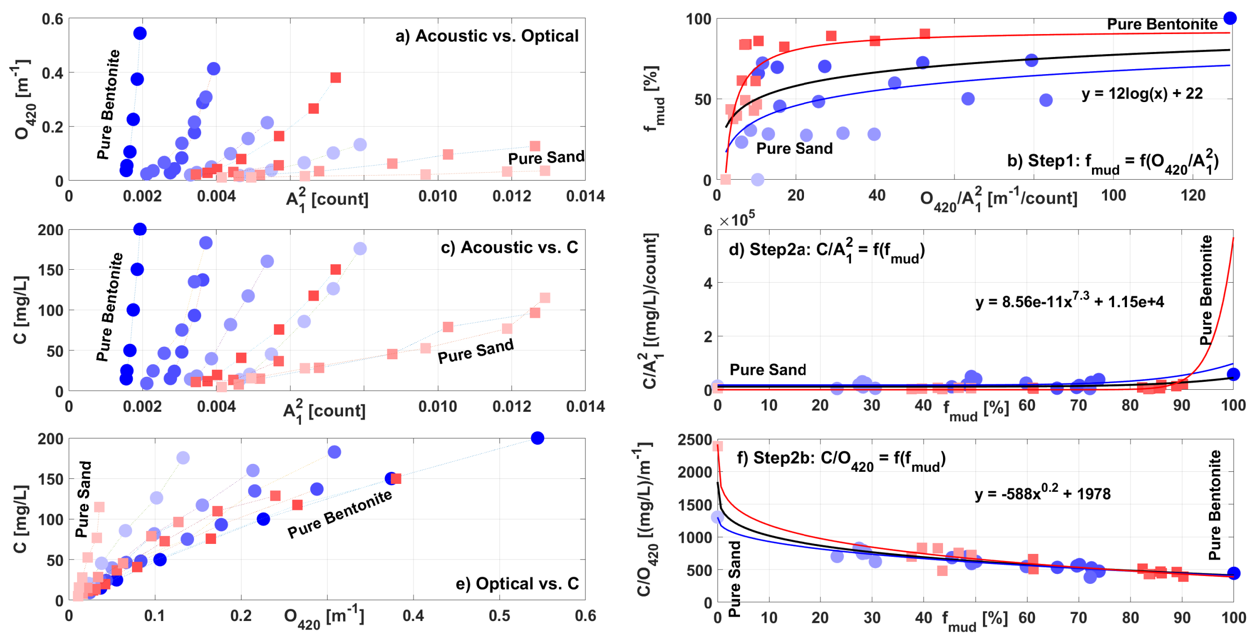

Figure B20: Application of SCI method to the optical/acoustic pair of $\mathbf{O}_{420}$ and $\mathbf{A}_1$ with data in C1 (blue), C2 (red) and C12 (black). The reductions of f_{mud} from 100% to 0% are shown by the darkest color to lightest color. The displayed function are obtained from data set C12.

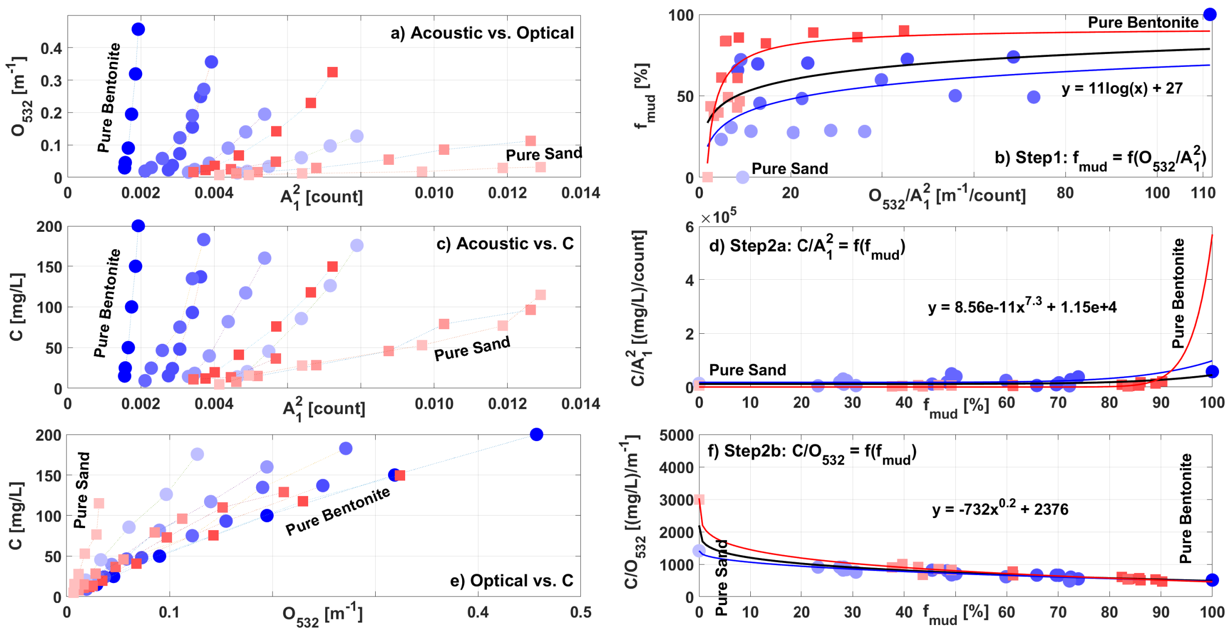

Figure B21: Application of SCI method to the optical/acoustic pair of $\mathbf{O}_{532}$ and $\mathbf{A}_1$ with data in C1 (blue), C2 (red) and C12 (black). The reductions of f_{mud} from 100% to 0% are shown by the darkest color to lightest color. The displayed function are obtained from data set C12.

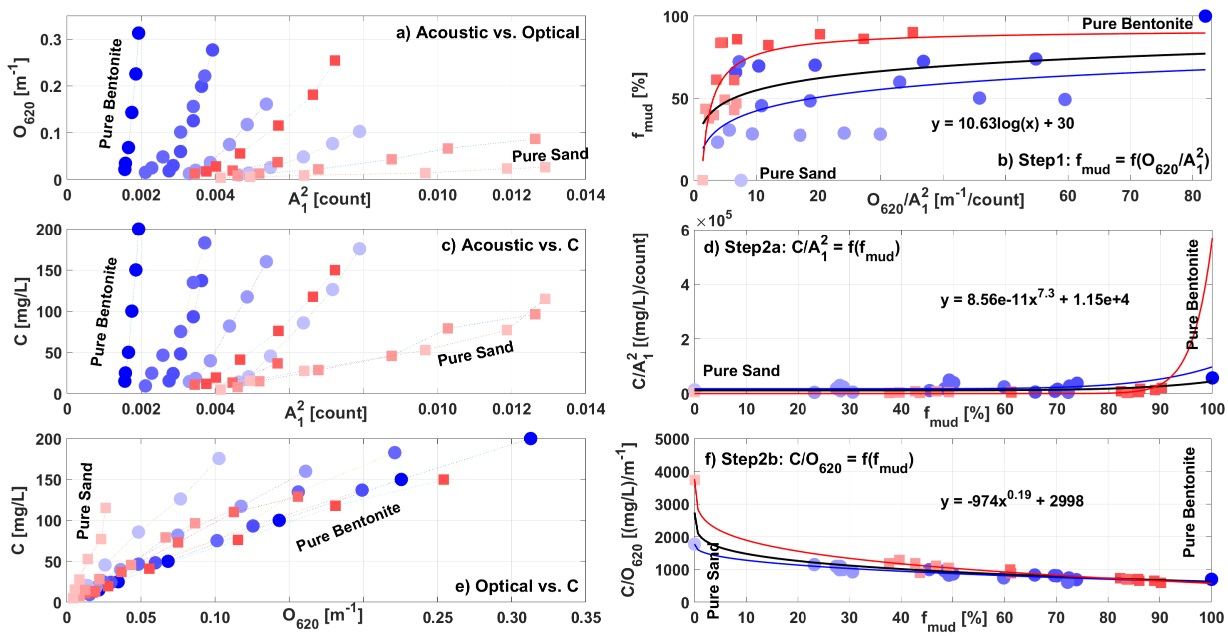

Figure B22: Application of SCI method to the optical/acoustic pair of $\mathbf{O}_{620}$ and $\mathbf{A}_1$ with data in C1 (blue), C2 (red) and C12 (black). The reductions of f_{mud} from 100% to 0% are shown by the darkest color to lightest color. The displayed function are obtained from data set C12.

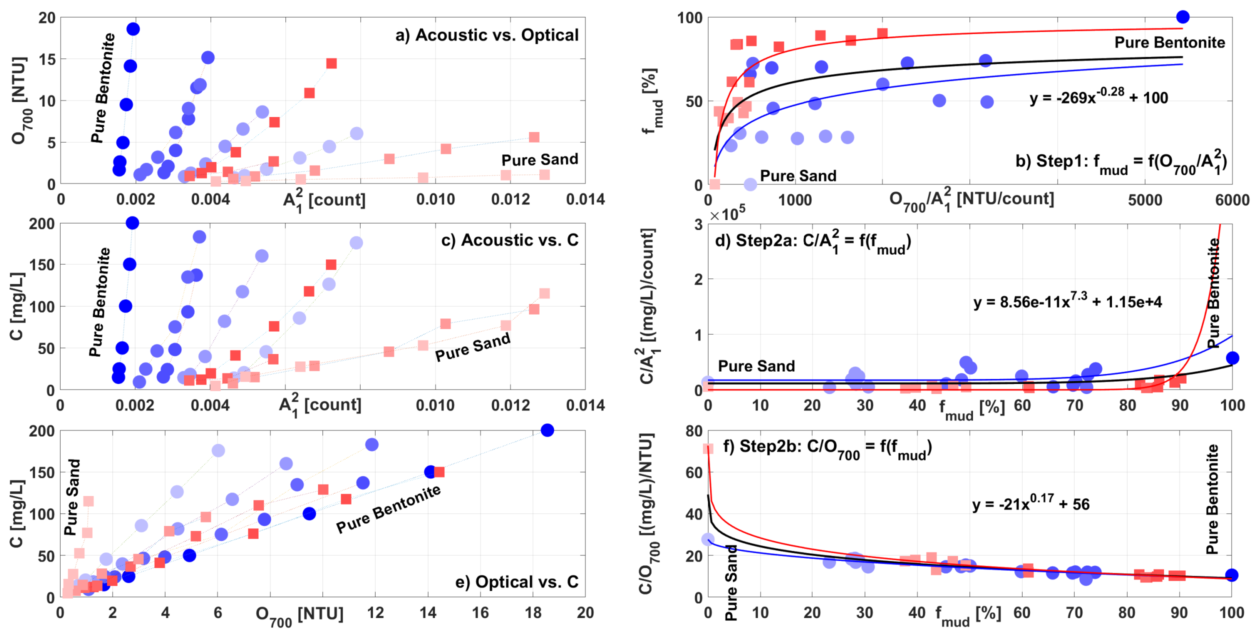

Figure B23: Application of SCI method to the optical/acoustic pair of $\mathbf{O}_{700}$ and $\mathbf{A}_1$ with data in C1 (blue), C2 (red) and C12 (black). The reductions of f_{mud} from 100% to 0% are shown by the darkest color to lightest color. The displayed function are obtained from data set C12.

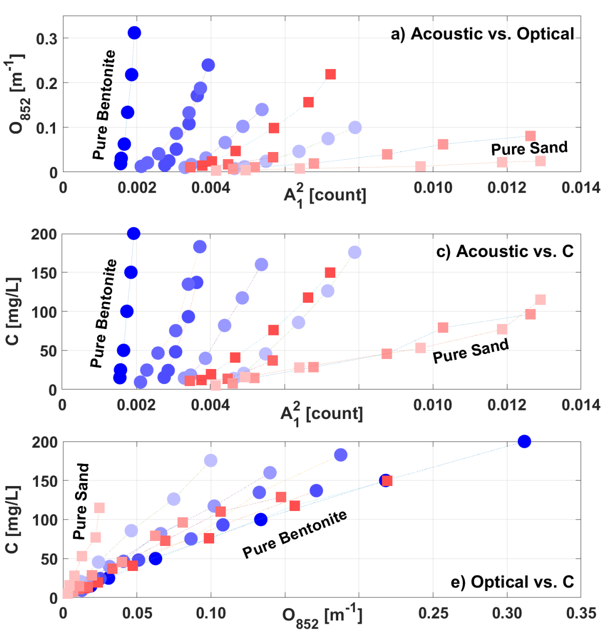

Figure B24: Application of SCI method to the optical/acoustic pair of $\mathbf{O}_{852}$ and $\mathbf{A}_1$ with data in C1 (blue), C2 (red) and C12 (black). The reductions of f_{mud} from 100% to 0% are shown by the darkest color to lightest color. The displayed function are obtained from data set C12.

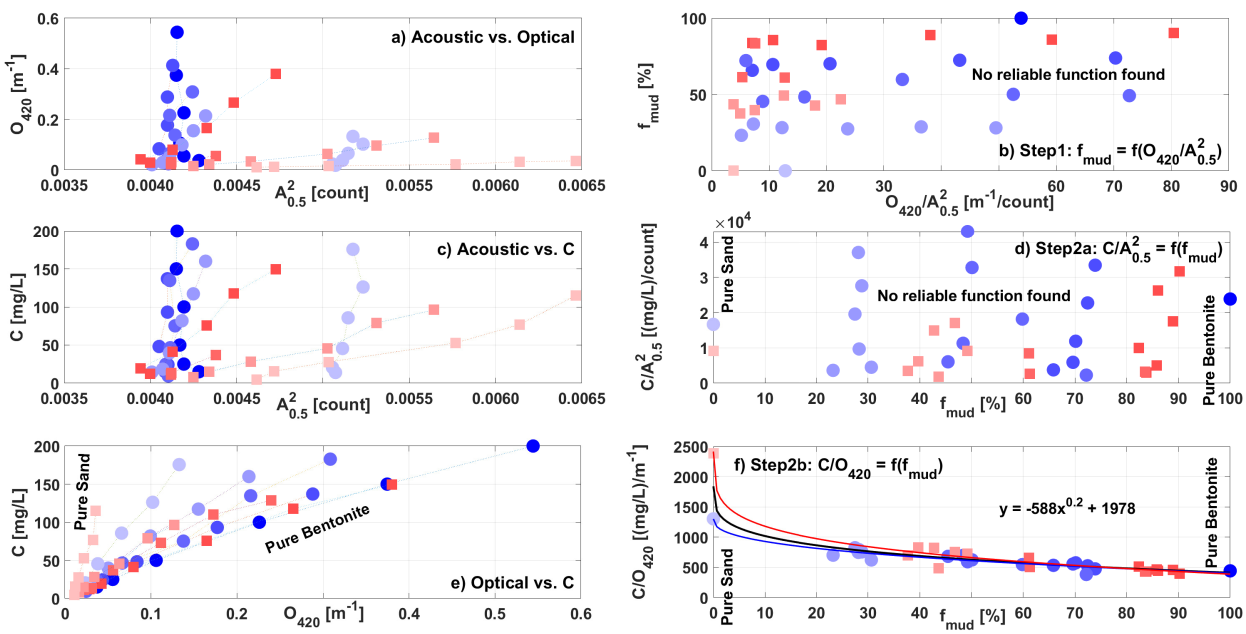

Figure B25: Application of SCI method to the optical/acoustic pair of $\mathbf{O}_{420}$ and $\mathbf{A}_{0.5}$ with data in C1 (blue), C2 (red) and C12 (black). The reductions of f_{mud} from 100% to 0% are shown by the darkest color to lightest color. The displayed function are obtained from data set C12.

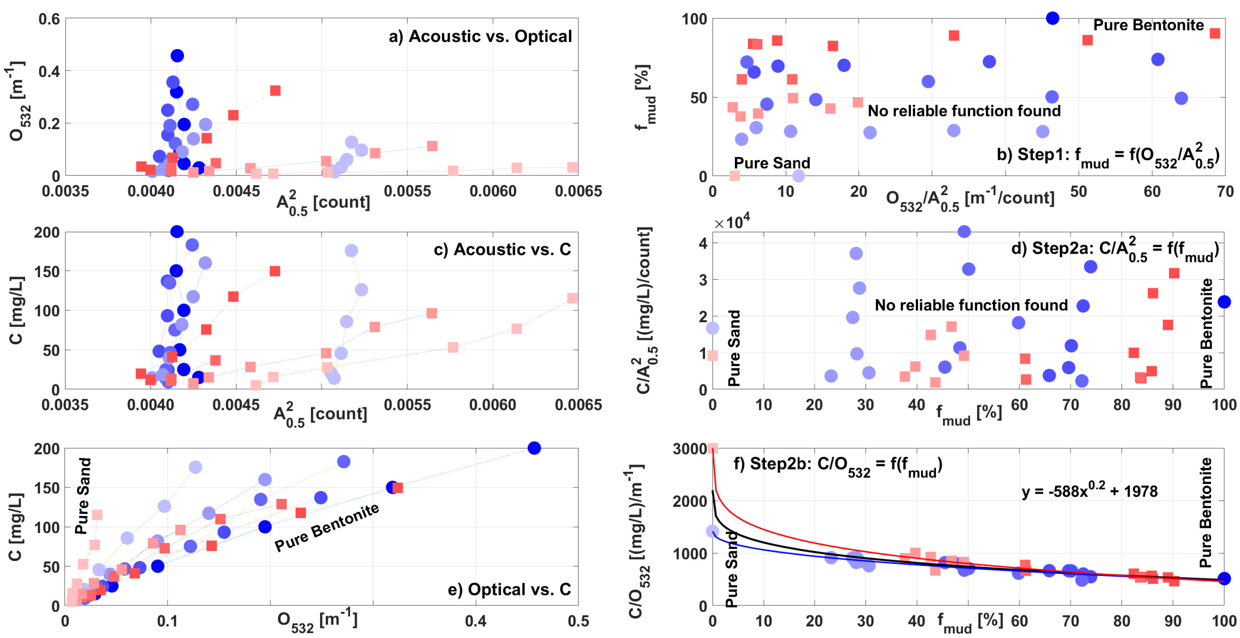

Figure B26: Application of SCI method to the optical/acoustic pair of $\mathbf{O}_{532}$ and $\mathbf{A}_{0.5}$ with data in C1 (blue), C2 (red) and C12 (black). The reductions of f_{mud} from 100% to 0% are shown by the darkest color to lightest color. The displayed function are obtained from data set C12.

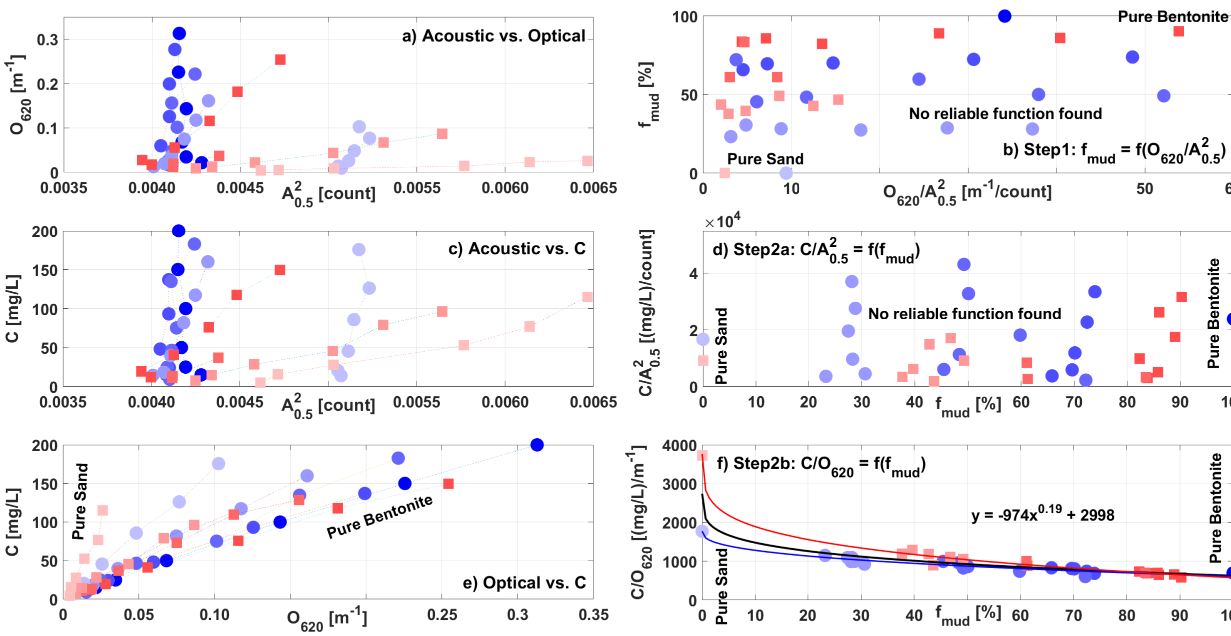

Figure B27: Application of SCI method to the optical/acoustic pair of $\mathbf{O}_{620}$ and $\mathbf{A}_{0.5}$ with data in C1 (blue), C2 (red) and C12 (black). The reductions of f_{mud} from 100% to 0% are shown by the darkest color to lightest color. The displayed function are obtained from data set C12.

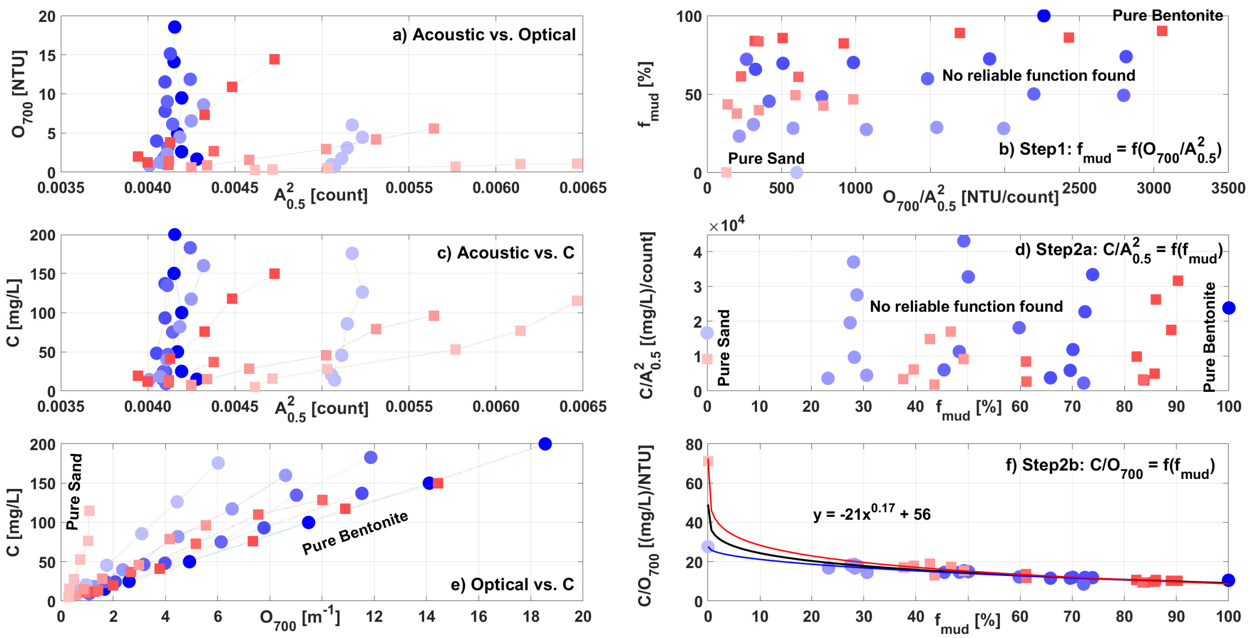

Figure B28: Application of SCI method to the optical/acoustic pair of $\mathbf{O}_{700}$ and $\mathbf{A}_{0.5}$ with data in C1 (blue), C2 (red) and C12 (black). The reductions of f_{mud} from 100% to 0% are shown by the darkest color to lightest color. The displayed function are obtained from data set C12.

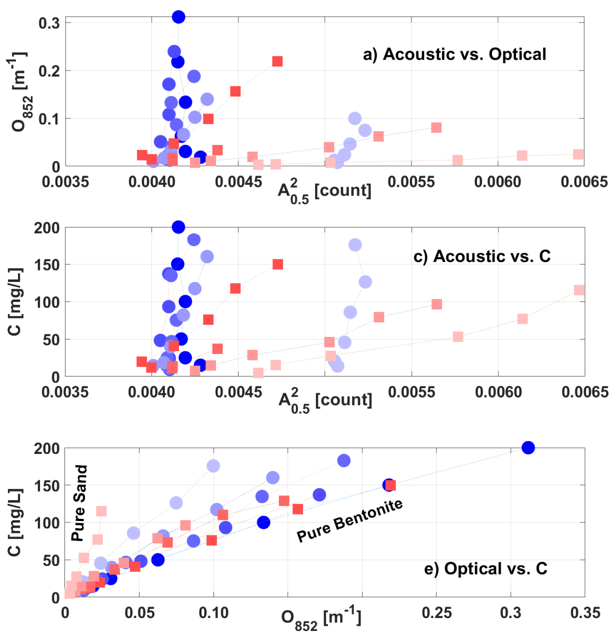

Figure B29: Application of SCI method to the optical/acoustic pair of $\mathbf{O}_{852}$ and $\mathbf{A}_{0.5}$ with data in C1 (blue), C2 (red) and C12 (black). The reductions of f_{mud} from 100% to 0% are shown by the darkest color to lightest color. The displayed function are obtained from data set C12.

References

Aquatec Subsea Ltd (2012). Application Note AN4 - inversion technique. AN4Rev1.0.

Bux, J., Peakall, J., Rice, H. P., Manga, M. S., Biggs, S., and Hunter, T. N. (2019). Measurement and density normalisation of acoustic attenuation and backscattering constants of arbitrary suspensions within the rayleigh scattering regime. *Applied Acoustic*, 146:9 – 22.

Chmiel, O., Baselt, I., and Malcherek, A. (2018). Applicability of acoustic concentration measurements in suspensions of artificial and natural sediments using an acoustic doppler velocimeter. *Acoustics*, 1(1):59–77.

Downing, J. (2006). Twenty-five years with OBS sensors: The good, the bad, and the ugly. *Continental Shelf Research*, 26(17):2299–2318.

Doxaran, D., Leymarie, E., Nechad, B., Dogliotti, A., Ruddick, K., Gernez, P., and Knaeps, E. (2016). Improved correction methods for field measurements of particulate light backscattering in turbid waters. *Optics Express*, 24(4):3615.

Druine, F., Verney, R., Deloffre, J., Lemoine, J., Chapalain, M., Landemaine, V., and Lafite, R. (2018). In situ high frequency long term measurements of suspended sediment concentration in turbid estuarine system (seine estuary, france): Optical turbidity sensors response to suspended sediment characteristics. *Marine Geology*, 400:24–37.

Fettweis, M., Riethmüller, R., Verney, R., Becker, M., Backers, J., Baeye, M., Chapalain, M., Claeys, S., Claus, J., Cox, T., Deloffre, J., Depreiter, D., Druine, F., Flöser, G., Grünler, S., Jourdin, F., Lafite, R., Nauw, J., Nechad, B., Röttgers, R., Sottolichio, A., Van Engeland, T., Vanhaverbeke, W., and Vereecken, H. (2019). Uncertainties associated with in situ high-frequency long-term observations of suspended particulate matter concentration using optical and acoustic sensors. *Progress in Oceanography*, 178:102162.

Haalboom, S., de Stigter, H., Duineveld, G., van Haren, H., Reichart, G. J., and Mienis, F. (2021). Suspended particulate matter in a submarine canyon Whittard Canyon, Bay of Biscay, NE Atlantic Ocean : Assessment of commonly used instruments to record turbidity. *Marine Geology*, 434:106439.

Hoitink, A. and Hoekstra, P. (2005). Observation of suspended sediment from adcp and obs measurements in a mud-dominanted environment. *Coastal Engineering*, 52(2):103–118.

Livsey, D. N., Turner, R. D. R., and Grace, P. R. (2023). Combining optical and acoustic backscatter measurements for monitoring of fine suspended-sediment concentration under changes in particle size and density. *Water Resources Research*, 59(8):1–20.

Lynch, J. F., Irish, J. D., Sherwood, C. R., and Agrawal, Y. C. (1994). Determining suspended sediment particle size information from acoustical and optical backscatter measurements. *Continental Shelf Research*, 14(10-11):1139–1165.

Moate, B. D. and Thorne, P. D. (2009). Measurements and inversion of acoustic scattering from suspensions having broad size distributions. *Journal of the Acoustical Society of America*, 126(6):2905 – 2917.

Moura, M. G., Quaresma, V. S., Bastos, A. C., and Veronez, P. (2011). Field observations of SPM using ADV, ADP, and OBS in a shallow estuarine system with low SPM concentration-Vitória Bay, SE Brazil. *Ocean Dynamics*, 61(2-3):273–283.

Pearson, S. G., Verney, R., van Prooijen, B. C., Tran, D., Hendriks, E. C., Jacquet, M., and Wang, Z. B. (2021). Characterizing the composition of sand and mud suspensions in coastal and estuarine environments using combined optical and acoustic measurements. *Journal of Geophysical Research : Oceans*, 126:e2021JC017354.

Sahin, C., Verney, R., Sheremet, A., and Voulgaris, G. (2017). Acoustic backscatter by suspended cohesive sediments : Field observations, seine estuary, france. *Continental Shelf Research*, 134:39–51.

Salehi, M. and Strom, K. (2011). Using velocimeter signal to noise ratio as a surrogate measure of suspended mud concentration. *Continental Shelf Research*, 31(9):1020–1032.

Slade, W. H., Boss, E., and Russo, C. (2011). Effects of particle aggregation and disaggregation on their inherent optical properties. *Optics Express*, 19(9):7945–7959.

Sutherland, T. F., Lane, P. M., Amos, C. L., and Downing, J. (2000). The calibration of optical backscatter sensors for suspended sediment of varying darkness levels. *Marine Geology*, 162(2-4):587–597.

Thorne, P. D. and Hurther, D. (2014). An overview on the use of backscattered sound for measuring suspended particle size and concentration profiles in non-cohesive inorganic sediment transport studies. *Continental Shelf Research*, 73:97–118.

Thorne, P. D., Lichtman, I. D., and Hurther, D. (2021). Acoustic scattering characteristics and inversions for suspended concentration and particle size above mixed sand and mud beds. *Continental Shelf Research*, 214:104320.

Tran, D., Jacquet, M., Pearson, S., and Verney, R. (2021). Investigating suspended particulate matters from multi-wavelength optical and multi-frequency acoustic measurements. *EGU 2021*, page 13022.